journal of the international meteor organization

WGN

43:4
august 2015

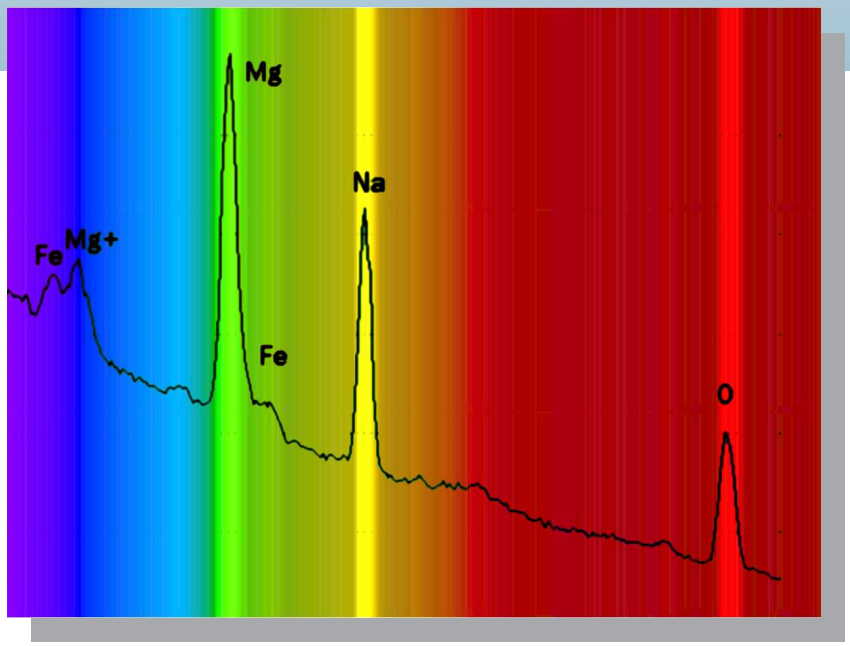

Meteor spectroscopy special issue:

- Method for the analysis of meteor spectra
- Spectroscopy of the Quadrantids
- Spectroscopic and multi-station observations combined

March–April video meteors

ISSN 1016-3115

WGN Vol. 43, No. 4, August 2015, pp. 93 – 120

Administrative

Meteor Science

Preliminary results

Front cover photo

Spectrum graph overlaid on colourised synthetic spectrum from a meteor captured from Kilwinning, Scotland on 2015 April 10 at $00^{h}58^{m}37^{s}$ UT. See page 106 for details. Image courtesy: William Ward.

Writing for WGN

This Journal welcomes papers submitted for publication. All papers are reviewed for scientific content, and edited for English and style. Instructions for authors can be found in WGN **31:4**, 124–128, and at `http://www.imo.net/docs/writingforwgn.pdf` .

Legal address

International Meteor Organization, Jozef Mattheessensstraat 60, 2540 Hove, Belgium.

Letter — Meteoroid "family groups"

Bill Ward[1]

In several years of regular video meteor spectroscopy I have captured many varied spectra. The usual elements appear in them all. With the exception of spectra obtained from showers, they have all shown subtle variations. The spectra from shower meteors do show variations in line intensities but the spectrum patterns are the same. This seems reasonable if it is assumed they have a common parentage.

However after reading a posting by Martin Dubs (Switzerland) on the *UFO Capture forum*[a] it occurred to me that a milestone of sorts had now been reached. Martin was enquiring as to the line identification of a spectrum he had captured (Figure 1).

To me, what those lines actually were did not seem as significant as compared to the overall spectrum pattern! I had caught a good spectrum of a sporadic meteor a short while ago (Figure 2). It is clear that both spectra are more or less identical. This immediately brought about some thoughts. Firstly is that they are made from the same material, perhaps not that unusual but I am not aware of any other sporadic meteor spectrum which has such similar characteristics to another. (if anyone has or knows of others please let me know. This will add evidence to the case!) Secondly, does this mean that these two meteoroids may have the same source in terms of solar system history? And thirdly, are there distinct "family groups" within meteoroids that can be identified through spectroscopy?

For example there are some 14 categories of meteorite families known. Will long term meteor spectroscopy reveal this sort of number? Not only that, video meteor spectroscopy allows us to look at cometary material also. There are no large collections of this available for laboratory analysis!

From my own experience in a VERY cloudy part of the world the return on observing time is low for meteor spectroscopy when compared to ordinary video observations BUT it can be done. Therefore I would encourage those observers who have multiple cameras to consider dedicating one to spectroscopy. It may very well take a long time but I believe it has got to be worth it. It is only at this point in time that we now have the tools to even think about such issues.

Video meteor spectroscopy continues to develop as a powerful tool and we might have just taken the very first step into a new taxonomy for meteors and meteor observing.

IMO bibcode WGN-434-ward-letter NASA-ADS bibcode 2015JIMO...43...93W

Figure 1 – Spectrum captured by Martin Dubs on 2015 June 25 at $22^{h}09^{m}37^{s}$ UT.

Figure 2 – Spectrum captured by Bill Ward on 2015 April 23 at $00^{h}55^{m}21^{s}$ UT.

[1] Email: William.Ward@glasgow.ac.uk

[a] http://sonotaco.jp/forum/viewtopic.php?t=3065&start=60

Meteor Science

A practical method for the analysis of meteor spectra

Martin Dubs[1] *and Peter Schlatter*[2]

The analysis of meteor spectra (photographic, CCD or video recording) is complicated by the fact that spectra obtained with objective gratings are curved and have a nonlinear dispersion. In this paper it is shown that with a simple image transformation the spectra can be linearized in such a way that individual spectra over the whole image plane are parallel and have a constant, linear dispersion. This simplifies the identification and measurement of meteor spectral lines. A practical method is given to determine the required image transformation.

Received 2015 May 21

1 Introduction

Meteor spectra are recorded by placing a prism or a transmission grating in front of the camera lens (Rendtel, 2002). The light of any point source is separated into a line spectrum, with different wavelengths refracted or diffracted at different angles. In prisms, the wavelength separating mechanism is refraction, which is highly nonlinear. This is described by the dispersion $\mathrm{d}\beta/\,\mathrm{d}\lambda$, the change in refraction angle per wavelength unit. It is a strongly varying function of the wavelength λ and depends on the prism angle and prism material. In gratings the separation of different wavelengths is caused by diffraction from the closely spaced grating lines and dispersion is a slowly varying function of the incident and exit angles and inversely proportional to the separation of grating lines.

There are other differences between prisms and gratings. Prism angular dispersion is generally small, requiring long focal lengths for sufficient linear dispersion. An advantage of prisms is that all light is separated into one spectrum. Gratings on the other hand produce spectra of different orders with different dispersion. Part of the light passes through the grating undiffracted (the so called zero order), which is used as a zero wavelength reference. If recorded, this is of great help for the calibration of the spectrum. Modern gratings are blazed, that means that most of the light is diffracted into one (often the first) order with an efficiency of typically 50% or higher. The rest of the light produces the zero order and other (higher) orders on both sides of the zero order.

In this paper only grating spectra are discussed, as they are at present the preferred choice for video and CCD cameras with a small chip size (compared to large size photographic film). Unfortunately the same method cannot be applied to prism spectra, where the nonlinearities are much greater and of a different origin.

For a given chip size the focal length of the lens determines the field of view and for a given grating also the linear dispersion $\mathrm{d}x/\,\mathrm{d}\lambda$ in μm/nm or pixel/nm. As the light of a meteor is dispersed over many pixels the detection sensitivity is several magnitudes lower for meteor spectra than for the detection of meteors with the same lens detector combination, so fewer meteors are recorded. Choosing a short focal length increases the field of view but reduces the linear dispersion or resolution of the spectrum. In addition, at larger incident and diffracted angles the nonlinearity of dispersion becomes more apparent, making the analysis of spectra quite complicated. Both, the low number of useful events and the complicated analysis of the spectra discourages many observers of recording meteor spectra.

In this paper, the calibration of meteor spectra is treated in some detail. Based on simple geometric analysis a practical method is given which straightens the curved, nonlinear spectra to parallel, linear spectra with constant dispersion over the whole field of view. The geometric approach also suggests a method for determining the required image transformation, which will be discussed in detail below.

2 Theory of grating diffraction

A method for computing the wavelengths of objective grating spectra, suitable for analysis of meteor spectra, is described in (Ceplecha, 1961). At the time the Ceplecha paper had been written, computers were not in widespread use and photographic film was the recording medium. Today software for image analysis and CCDs are in common use and the analysis of the spectra should take advantage of the increased possibilities. For easier comparison with that work, the same notation and coordinate systems as far as convenient will be used in the present paper.

Figure 1 shows the orientation of a Cartesian coordinate system with respect to the grating. The plane of the grating coincides with the xy-plane and the grooves are aligned parallel to the y-axis. Light from a meteor trail can be regarded as a succession of point sources at infinity, each point being characterized by parallel rays that eventually impinge on the grating. In the given coordinate system, the components of a unit vector (A, B, C) describe the direction of the rays originating from one point, while the components of the unit vector (A', B', C') describe the direction of the diffracted

[1]Im untern Stieg 2, CH-7304 Maienfeld, Switzerland.
Email: martin-dubs@bluewin.ch
[2]Birkenweg 8, CH-3033 Wohlen b. Bern, Switzerland

IMO bibcode WGN-434-dubs-spectra
NASA-ADS bibcode 2015JIMO...43...94D

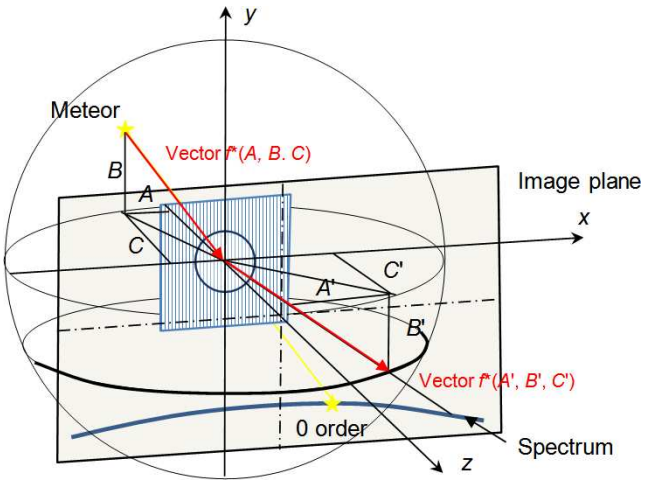

Figure 1 – Coordinate system. (A, B, C) components of incident ray unit vector. (A', B', C'): components of diffracted ray unit vector, projected on a sphere with radius f.

beam. The grating equation relates these two vectors (Rowland, 1893):

$$A' = A + m\lambda G \tag{1}$$

$$B' = B \tag{2}$$

$$C' = \sqrt{(1 - A'^2 - B'^2)} \tag{3}$$

λ denotes the wavelength of the incident beam and m is the grating order. The special case $m = 0$ is called zero order, for which the incident beam is not deflected, independent of the wavelength. G is the grating constant or inverse grating line-spacing in grooves/mm.

In textbooks on optics, the grating equation is usually given in angular notation, see e.g. (Schroeder, 1970):

$$m\lambda G = \cos\gamma(\sin\beta + \sin\alpha) \tag{4}$$

with α denoting the angle of incidence, β the angle of diffraction and γ the angle between the incident ray and the xz-plane. While the angular notation is equivalent to the vector notation of equations (1–3), the vector notation considerably facilitates the subsequent derivations.

3 A basic lens model

The orientation of the meteor camera relative to the coordinate system is shown in Figure 2. The optical axis of the lens is coincident with the z-axis and both the image plane and the grating plane are at right angles to the z-axis. In order to find the image point P of the diffracted ray (A', B', C'), a basic model of the lens is required. If we assume that the lens is free of aberrations except distortion, there is rotational symmetry with respect to the optical axis. Then, the distance r of an image point P from the optical axis is entirely determined by the angle between the diffracted ray and the z-axis, the polar angle ρ:

$$r = fg(\rho) \tag{5}$$

where f denotes the focal length of the lens. The function $g(\rho)$ determines the projection properties of the

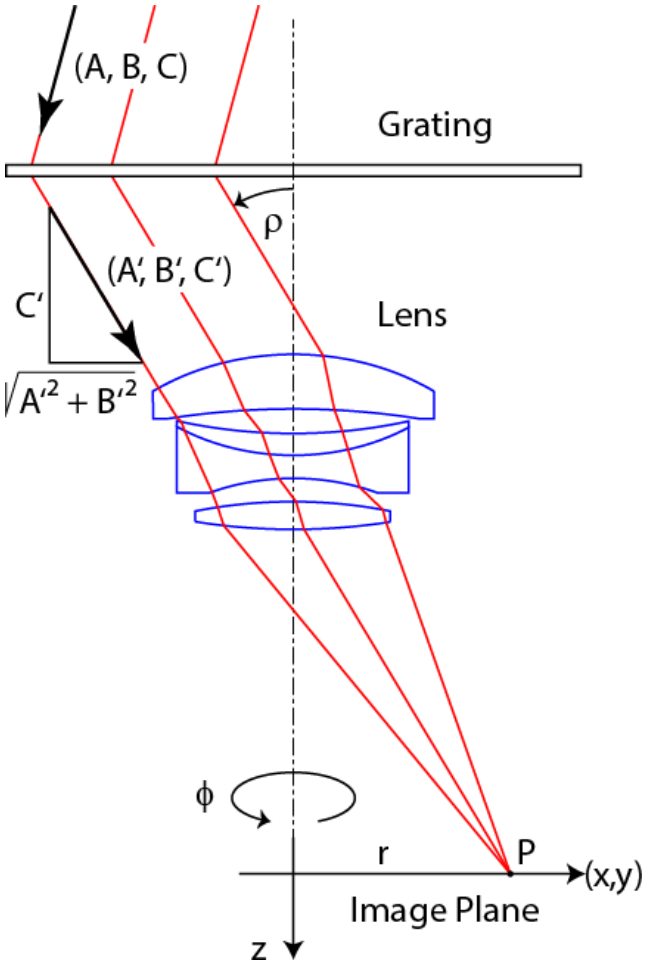

Figure 2 – Section through meteor camera showing relation between ρ and r.

lens. It must be an odd, strictly increasing function, and for small angles of ρ, i.e. for paraxial rays, $g(\rho) = \rho$. A Taylor expansion will consist of terms with odd exponents only. An ideal lens, for example, is characterized by the so called gnomonic projection, for which $g(\rho) = \tan(\rho)$ (Calabretta & Greisen, 2002).

With equation (5), the coordinates of the image point P are given by

$$x = r\cos\phi = fg(\rho)\cos\phi \tag{6a}$$

$$y = r\sin\phi = fg(\rho)\sin\phi \tag{6b}$$

where ϕ refers to the azimuth angle of point P, measured in the xy-plane. Both the azimuth angle ϕ and the polar angle ρ may be expressed in terms of the unit vector (A', B', C'), see Figure 2:

$$\sin\rho = \sqrt{(A'^2 + B'^2)}$$

$$\cos\phi = A'/\sqrt{(A'^2 + B'^2)} = A'/\sin\rho$$

$$\sin\phi = B'/\sqrt{(A'^2 + B'^2)} = B'/\sin\rho$$

Substituting the last two equations into equations (6a) and (6b) and taking into account equations (1) and (2) leads to

$$x = fg(\rho)/\sin(\rho)(A + m\lambda G) \tag{7a}$$

$$y = fg(\rho)/\sin(\rho)B \tag{7b}$$

These two relations are valid for any lens with projection properties $g(\rho)$. They define how the rays of a point source in the sky at (A, B) are mapped to the sensor at (x, y).

A special choice for $g(\rho)$ is the orthographic projection. It is defined by $g(\rho) = \sin(\rho)$ (Calabretta & Greisen, 2002). Inserting this into equations (7a and 7b), the $\sin(\rho)$ term in the denominator and the explicit dependence of (x, y) on ρ are eliminated:

$$x = f(A + m\lambda G) \tag{8a}$$

$$y = fB, \tag{8b}$$

$$\mathrm{d}x/\,\mathrm{d}\lambda = fmG \tag{9}$$

The orthographic projection maintains the linearity of the vector components in equations (1) and (2), and a polychromatic point source is expanded into a spectrum with ideal properties:

- The spectrum extends along a straight line parallel to the x-axis.
- The linear dispersion has a constant value over the entire image plane. The dispersion may easily be determined from two known spectral lines or the zero order and one spectral line.
- Individual spectra of the points that make up a meteor trail are shifted in x and in y and are parallel to each other. Since the dispersion has a location-independent value, one global calibration suffices to reduce all spectra.

Unfortunately, lenses do not map objects according to an orthographic projection. Rather an ideal lens is characterized by the gnomonic projection, defined by $g(\rho) = \tan\rho$. Ceplecha's calculations are in fact based on an ideal lens. This leads to curved spectra, the so called "diffraction hyperbola" and to non-linear and location-dependent dispersion relations. But even high-quality lenses show some distortion and deviate from a gnomonic projection, thereby modifying the hyperbola in a complicated way. And particularly wide-angle lenses, which are popular in meteor cameras, are affected by distortion.

We now show that these difficulties can be avoided by applying an image transformation that radially distorts the image in such a way that the resulting projection becomes orthographic. After this transformation, equations (8) and (9) apply. The spectra are rectified and the dispersion gets constant over the entire field.

The required transformation maps a point in the original image, $P = (r, \phi)$, to a point in the radially modified image, $P' = (r', \phi)$. The azimuth angle ϕ is left unchanged and, by the definition of the orthographic projection, the transformed radius must satisfy the equation

$$r' = f\sin\rho \tag{10}$$

Inverting the function g in equation (5) and solving for the polar angle ρ leads to the prescription for the transformation:

$$r' = f\sin[g^{-1}(r/f)] \tag{11a}$$

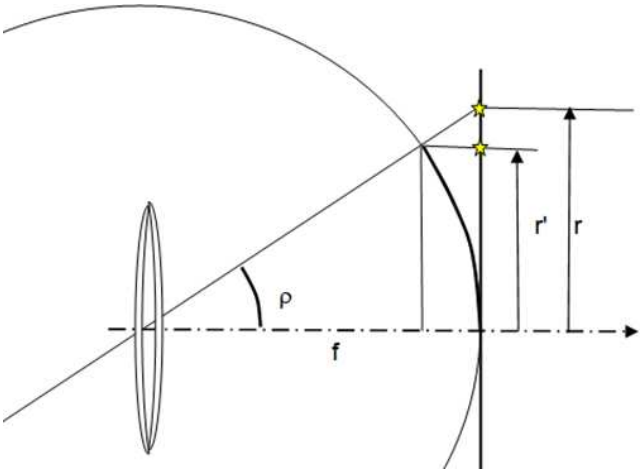

Figure 3 – Relation between the gnomonic projection (r) and the orthographic projection (r') of a point on the sphere with radius f. The prime denotes the coordinates in the orthographic projection coordinate system.

The inverse function

$$r = fg[\arcsin(r'/f)] \tag{11b}$$

is required for the practical calibration example and for the implementation of the transformation in an image processing software.

For the tangential (gnomonic) projection as a special case (no lens distortion) the transformation to the orthographic projection can be given in explicit form (see also Figure 3):

$$r = f\tan[\arcsin(r'/f)] = r'/\sqrt{[1-(r'/f)^2]} \tag{12}$$

The function $g(\rho)$, which is required for the transformation, must be determined experimentally for each lens/sensor combination. Several methods may be considered, e.g. an astrometric analysis of a star field or a direct measurement on an optical bench.

As will be shown in a practical example, it is possible to define the transformation without resorting to $g(\rho)$ by directly analyzing a calibration spectrum. This method relies on the fact that both $\sin(\rho)$ and $g(\rho)$ are odd functions. Equation (11b) can be represented by a polynomial with odd exponents in r/f:

$$r = f(r'/f + a_3(r'/f)^3 + a_5(r'/f)^5 + \ldots) = r'(1 + a_3(r'/f)^2 + a_5(r'/f)^4 + \ldots) \tag{13}$$

For the tangential projection the polynomial coefficients of equation (12) are given by

$$r = r'(1 + \frac{1}{2}(r'/f)^2 + \frac{3}{8}(r'/f)^4 + \frac{5}{16}(r'/f)^6 + \ldots) \tag{14}$$

4 Equipment

Before describing the experiments, an overview of the used equipment may be useful, although the method is applicable to any meteor camera with a grating, if some important details are taken into account (in particular, the grating has to be mounted perpendicularly to the optical axis).

The meteor station at Maienfeld is equipped with two Watec 902H2 ultimate video cameras, one operating for the Swiss Meteor Network and supplying data to the FMA (Fachgruppe Meteorastronomie) database. This has a Computar HG2610AFCS-HSP lens (f = 2.6 mm, $f/1.0$) for recording and measuring time resolved meteor tracks. Together with the other stations of the network this gives the information about meteor path, velocity and distance. Without this information, the spectra alone would be much less useful.

The second camera is equipped with a zoom lens (Tamron 12VG412ASIR 1/2", f: 4–12 mm, $f/1.2$) and with a blazed 300 l/mm grating (Thorlabs GT50-03, blaze angle 17.5°, 50 × 50 mm).[a]

The grating has been changed recently to a 600 l/mm grating, for which however not many useful results exist yet. The zoom lens is quite convenient. In order to test and optimize the method and capture numerous spectra a short focal length was used. For the analysis of the meteor spectra resolution was not sufficient, so the focal length was increased. With luck some nice spectra were recorded, but still of limited scientific value. The 600 l/mm grating doubles the resolution within the same field of view, producing usable meteor spectra.

5 Calibration

In general, neither the exact grating constant nor the focal length and the distortion coefficients are precisely known, so some way of calibration is necessary. In addition, the rotational symmetry of the distortion correction given by the equations (11–14) above is only valid if the grating is mounted perpendicularly to the optical axis, so some attention should be given to verify this. Also the position of the optical axis is generally not exactly in the centre of the detector but a few pixels offset in the x- and y-coordinate at (x_0, y_0). Notice also that image coordinates are usually measured in pixels, with the origin at a corner. This will be assumed in the following unless otherwise noted. The radius $r = \sqrt{(x - x_0)^2 + (y - y_0)^2}$ is also measured in pixels. The position of the optical axis on the image sensor can be determined before mounting the grating, by imaging the night sky, if necessary with stacking several images and finding an astrometric solution of the coordinates of the stars in the image. If the software UFO Capture[b] is used for the acquisition of the images and UFO Analyzer for the astrometric solution of the images, both the aspect ratio of the pixels and the coordinates of the optical axis are fitted in addition to distortion parameters. If other image acquisition software is used, it may be necessary to calculate them, depending on the form of the astrometric solution. If the software for the radial transformation according to equation (13) assumes square pixels, the image has to be stretched in the y-direction by the corresponding aspect ratio factor, otherwise the rotational symmetry is lost and the transformation will not be correct for all parts of the image.

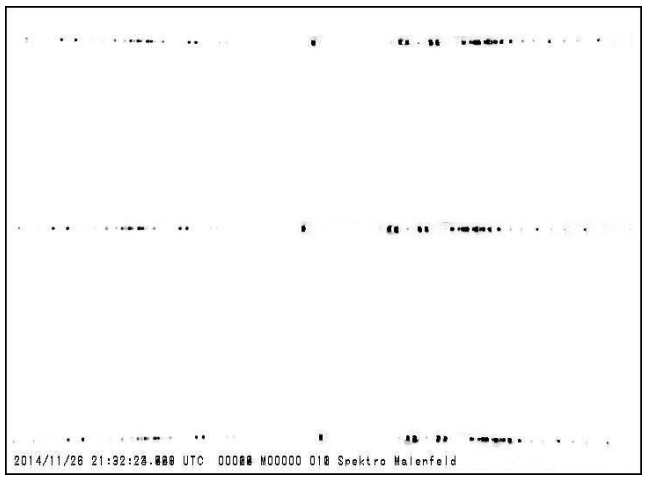

Figure 4 – Composite image of calibration lamp spectrum (Hg-Ar, Ocean Optics, orders −3 to 3) recorded in different parts of the image, superposed into a single image. Curvature is visible for the top and bottom spectra.

5.1 Calibration spectra

Depending on the desired accuracy several calibration spectra at different values of y should be recorded, stretching over the full width and height of the detector. In principle it is sufficient to record a calibration spectrum at $y = y_0$ (straight spectrum). For the calibration a suitable light source with lines with known wavelengths is used, which gives spectral lines over the whole width of the detector. For a start a monochromatic laser with known wavelength (e.g. He-Ne gas laser at 632.8 nm or a blue-ray laser at ≈ 405 nm) gives a course calibration of dispersion, in particular for wide angle lenses and/or gratings with low dispersion. Of course, higher order spectral lines should be used for the calibration as well, possibly taken with longer exposure times to see them. Quite useful is also an Hg-Ar calibration lamp[c] with several lines from UV to near-IR.

5.2 Calibration example

Figure 4 shows a composite image of a calibration lamp (Hg-Ar, Ocean Optics) recorded in the upper, centre and lower part of the image, combined into a single image. The image was corrected for the non-square pixel shape by a scaling factor of 0.9183 in the y-direction (obtained from an astrometric analysis of sky images in UFO Analyzer). The zoom lens was adjusted to approx. 7 mm focal length, the same as used for recording meteors in a longer detection run. Only the centre spectrum was used to determine the dispersion of the grating/lens combination and the transformation parameters for changing the actual image into an orthographic projection. A calibration function was fitted to the measured line positions with the method of least squares. The fitting function was obtained by using equation (8a), replacing x' by r' for $y = y_0$ and inserting r' into equation (12). The parameter c_2 was introduced

[a] http://www.thorlabs.de/newgrouppage9.cfm?objectgroup_id=1123

[b] http://sonotaco.com/soft/e_index.html

[c] http://oceanoptics.com/product/hg-1/

Table 1 – Measured positions of selected (non-overlapping) Hg lines in the central spectrum of Figure 4, together with calibration wavelengths (NIST)[e] in different orders and fitted positions according to equation (15).

m·λ_{NIST} [nm]	x [pixel]	fit x [pixel]	error [pixel]	Line
−1307.498	13.24	13.38	−0.14	Hg 3rd order
−1092.147	68.75	68.58	0.18	Hg 2nd order
−871.666	124.25	124.03	0.23	Hg 2nd order
−809.313	139.37	139.54	−0.17	Hg 2nd order
−546.074	204.43	204.41	0.02	Hg
−404.656	238.75	238.90	−0.16	Hg
0	336.80	336.80	−0.00	zero order
404.656	434.22	434.38	−0.16	Hg
546.074	468.83	468.62	0.21	Hg
809.313	532.87	532.77	0.09	Hg 2nd order
871.666	548.13	548.08	0.05	Hg 2nd order
1092.147	602.45	602.65	−0.20	Hg 2nd order
1307.498	656.77	656.72	0.00	Hg 3rd order

to account for lens distortion by interpolating between a gnomonic projection ($c_2 = (p/f)^2$) and an orthographic projection ($c_2 = 0$). This corrects for 3rd order lens distortion and gives a good approximation for the 5th order term:[d]

$$x = x_0 + (\lambda - \lambda_0)/disp_0/\sqrt{[1 - c_2((\lambda - \lambda_0)/disp_0)^2]} \quad (15)$$

($(\lambda-\lambda_0)/disp_0$ corresponds to $x'-x_0 = r'$ in the orthographic projection) with the following fit parameters: $disp_0 = (\mathrm{d}\lambda/\,\mathrm{d}x)_0 = 4.145$ nm/pixel (inverse dispersion), $x_0 = 362.2$ pixel, $\lambda_0 = 104.8$ nm (offset of λ at x_0), $c_2 = 4.104 \cdot 10^{-7}$.

The measured line positions together with the fitted positions used for the calibration are shown in Table 1.

From the inverse dispersion $(\mathrm{d}\lambda/\,\mathrm{d}x)_0$ and the known grating constant the focal length is calculated from equation (9) as $f = 6.92$ mm.

x_0 is the position determined for the symmetry centre of the fit function. Ideally it is located in the image centre, but small deviations may occur if the lens or the grating are not perfectly aligned.

From the fit parameters above, it is possible to calculate the distortion coefficients according to equation (13):

$$r = r'[1 + 2.052 \cdot 10^{-7} r'^2 + 6.318 \cdot 10^{-14} r'^4], \quad (16)$$

with r and r' measured from the apparent centre (x_0, y_0). The value of y_0 can be determined from the variation of the dispersion $(\mathrm{d}\lambda/\,\mathrm{d}x)_0$ as a function of y, by calibrating spectra at different y-values and determining its maximum. This is shown in Figure 5, with resulting values of $(x_0, y_0) = (362.2, 281.3)$.

With the position of the symmetry centre and the coefficients of equation (13), the distortion parameters

[d]The distortion correction with c_2 is similar to the fit of lens distortion by the law (Kwon et al., 2014) $r = k_1 \cdot \sin(\beta/k_2)$ with adjustable parameters k_1, k_2, which interpolates between orthographic ($k_2 = 1$) and equidistant ($k_2 \to \infty$) projection.

[e]NIST, Atomic spectra database, `http://physics.nist.gov/PhysRefData/ASD/lines_form.html`

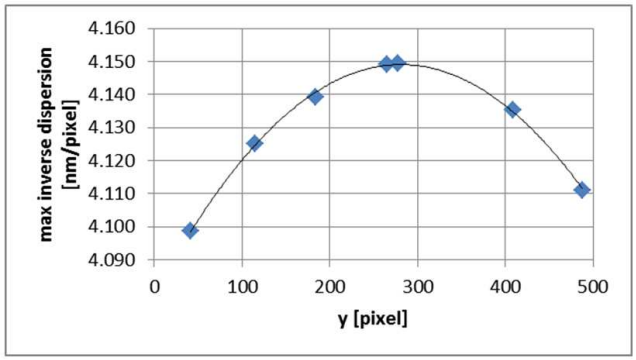

Figure 5 – Inverse dispersion from fit of measured spectra in different parts of the image.

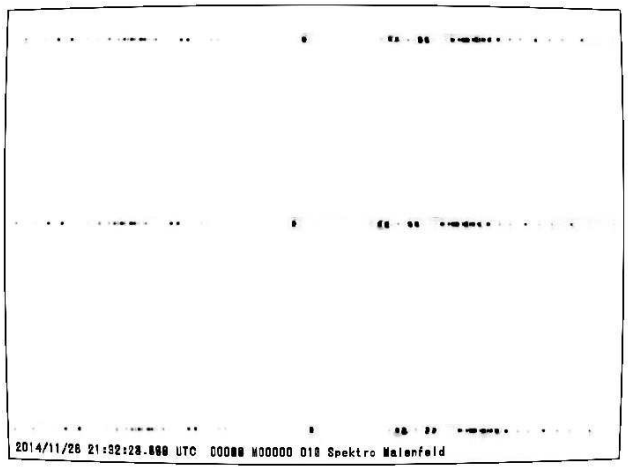

Figure 6 – Image of Figure 4, after applying the image transformation to correct the curvature of the spectrum and nonlinear dispersion.

of this lens are known and the transformation can be applied to the image of the spectrum, with the result shown in Figure 6. The slight curvature of the top and bottom spectrum is eliminated and the linearity of the calibration can be checked. With a single inverse dispersion of 4.145 nm/pixel, spectra for different y-values can be calibrated with an rms error of 0.94 nm or 0.23 pixel (Figure 7). The error is mostly caused by saturated spectral lines and only slightly larger than the rms error for a 5th order polynomial fit to the dispersion

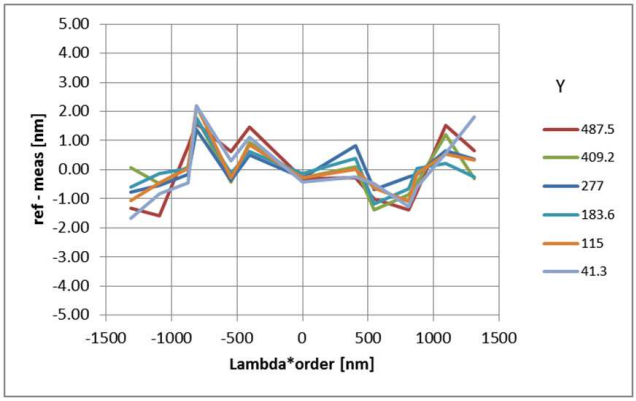

Figure 7 – Wavelength error of measured lines, compared to their computed position, assuming a constant dispersion of 4.145 nm/pixel for all the spectra.

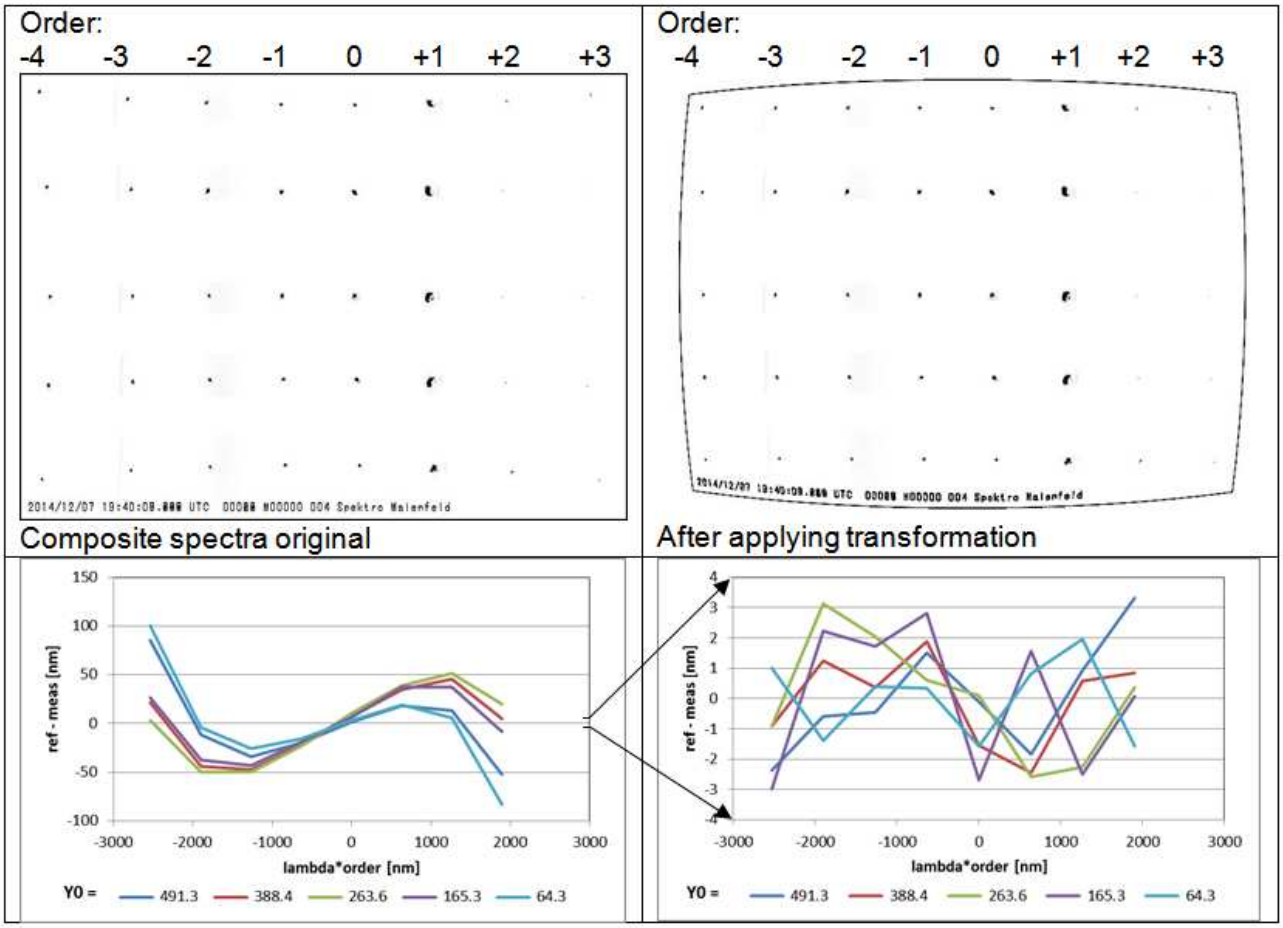

Figure 8 – Spectra before and after correction of grating nonlinearity and lens distortion. Left: Uncorrected data. Right: After application of the image transformation. Top: Spectra of He-Ne laser. Bottom: Errors from a calibration assuming a linear dispersion law. The blaze of the grating reduces the intensity of the 2nd and third order spectrum to $< 0.5\%$, making them barely visible, but sufficiently bright for analysis, while the first order is overexposed.

function of a single spectrum before applying the transformation. In addition the data show that in the corners the errors are largest. This is to be expected since the fit was done on the x-axis out to a radius of 360 pixel, with the half diagonal of 446 pixel being considerably larger. The fit could be improved by simultaneously fitting several spectra at different y values or by a separate determination of lens distortion. This was not done here.

5.3 2nd example, short focal lens, not useful for meteor spectroscopy

The following example, although not of practical value for meteor spectroscopy (too low spectral resolution), shows the effect of grating nonlinearity and lens distortion. The images were recorded with the same equipment as the example above, the difference being a shorter focal length (approx. 4 mm) and a He-Ne laser for calibration. At this wide angle enough orders of the He-Ne laser line at 632.8 nm are recorded for a symmetric 5th order polynomial fit of x vs. λ around x_0. The images before and after correction of distortion are shown in Figure 8. The coefficients for the correction of the distortion were: $(x_0, y_0) = (367.0, 286.5)$, $disp_0 = 7.354$ nm/pixel $\rightarrow f = 3.97$ mm, $r = r'[1 + 3.94 \cdot 10^{-7} r'^2 + 2.01 \cdot 10^{-12} r'^4]$. The rms error of the linear calibration after the transformation was 1.7 nm or 0.24 pixel.

6 Analysis of meteor spectra

Once calibrated and without changing grating orientation or focal length of the lens, spectra of meteors can be analysed with the following procedure.

- For video spectra the file is converted to single images. If desired, the video frames of an interlaced video may be deinterlaced into fields with higher time resolution. This results in higher spectral resolution, if the meteor velocity has a component in the direction of the dispersion (along x-axis).
- Dark frames are subtracted. A master dark can be obtained by averaging images before or after the appearance of the meteor. This subtraction also eliminates background stars, which otherwise could contaminate the meteor spectra.
- These images are stretched in the y-direction if necessary to produce square pixels. Then the transformation to the orthographic projection is applied to all images with meteor spectra. In a streamlined workflow, the image extraction from the video file with or without deinterlacing, the

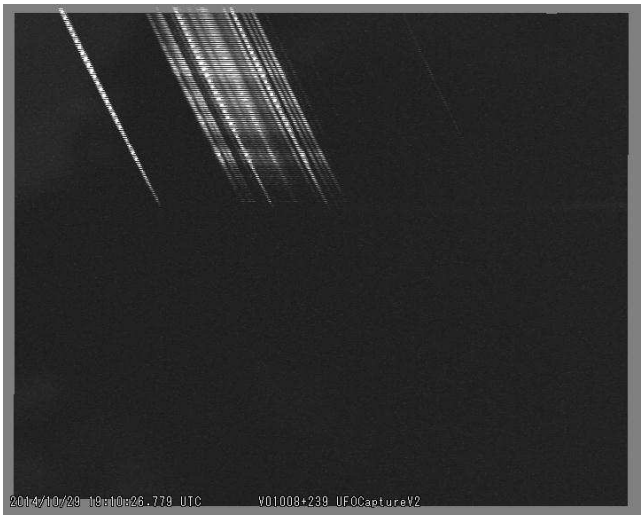

Figure 9 – Meteor 2014 October 29, $19^h10^m26^s$ UT at Maienfeld, peak image of video, duration of recorded path 0.68 sec, grating 300 l/mm.

stretching and transformation to the orthographic projection can be combined into a single procedure.

- The meteor spectra, because they are parallel and all have the same dispersion, can be stacked with the zero order as a suitable reference in order to increase signal to noise ratio. In case the zero order is not visible, another prominent line of the spectrum can be used as reference for stacking. Many video cameras only have 8-bit resolution, so averaging several frames is quite important.

- The resulting spectral image is converted to a 1-dimensional raw spectrum and calibrated with the known dispersion from the lamp calibration, using the zero order as a reference. As a check some well-known lines (e.g. Na-D or O I) should show up with the correct wavelength. Minor adjustments of calibration to compensate for a shift of focal length may be applied at this point. In the absence of the zero order (outside of image) the constant linear dispersion of the spectrum helps to identify some known meteor spectral lines and find the wavelength reference position. A correct line assignment of an unknown spectrum with not well known dispersion would be quite difficult.

- If available, the spectrum may be corrected for spectral response obtained from a spectrum of a light source with known spectral energy distribution (calibrated star or tungsten lamp with known blackbody temperature).

6.1 Meteor spectrum of 2014 October 29

The meteor of 2014 October 29, $19^h10^m26^s$ UT was selected as an example. It appeared right in the corner of the field of view, so the required distortion correction was the maximum possible (Figure 9). Peak magnitude of the meteor was −4.9 mag, with the zero order and the

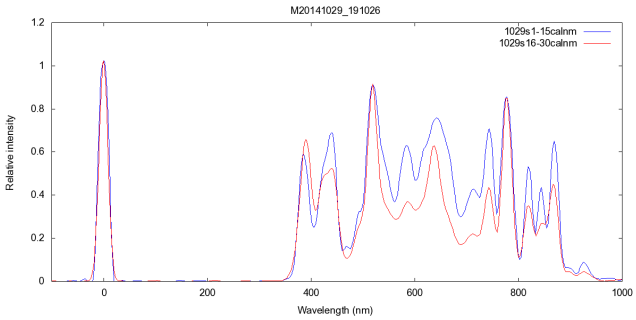

Figure 10 – Calibrated spectrum, blue curve: 1st part, video fields 54–68 of orthographic projection registered and stacked (average magnitude −4.7 mag). Red curve: 2nd part, video fields 69–83 (average magnitude −3.7 mag). Strong lines including zero order are broadened by saturation, especially in the first spectrum.

strongest lines overexposed due to the limited dynamic range of the video camera, which reduces the usability for a quantitative analysis of the intensities. The spectra of the individual video frames were processed as described above. After de-interlacing 30 spectra were dark corrected, transformed to the orthographic projection, and registered to align to the zero order. Two series of 15 spectra each were stacked. From these images the 1-dimensional spectra were extracted and calibrated with the zero order and the known inverse dispersion of 4.145 nm/pixel, verified by the O I lines at 777.4 nm in first and second order.

7 Conclusion

Meteor spectra do appear anywhere in the field of view, so the assignment of spectral lines may be difficult if the exact dispersion of the spectrum is not known and varies in different areas of the image. Using the described transformation of the spectra to an orthographic projection solves this problem. With the known wavelength of a single spectral line (e.g. the Na-D line), the whole spectrum can be calibrated for any position of the meteor in the image area. This is particularly useful if the zero order is outside the field of view. The determination of the transformation coefficients requires some effort, but it has to be done only once for each lens (at fixed focal length and fixed grating orientation). The transformation to a constant, linear scale without curvature allows using standard spectroscopy software for further analysis. The method has been shown to work with a short focal length camera, but it is applicable to larger format, longer focal length cameras with higher spectral resolution. To the knowledge of the authors, the use of the orthographic projection for linearization of spectral dispersion has not been applied to optical spectroscopy so far. In radio interferometry however, the orthographic projection is widely used in aperture synthesis (Calabretta, 2002). The transformation equations (11) to (14) are independent of the grating, they only depend on the lens and its distortions. Therefore the distortion coefficients can be derived without grating from an astrometric analysis of an image containing a sufficiently large number of stars. This is the

preferred method, as the whole field of view out to the corners contributes to the determination of the parameters. The dispersion can then be obtained from any two lines in the transformed image of a spectrum. The first results show that the method works as expected. Some improvements are still possible, such as the use of a grating with higher dispersion (first results look promising with increased resolution), or a camera with higher angular resolution and larger dynamic range. The software can also be streamlined to simplify the processing of the video files into calibrated spectra.

Acknowledgments

This project is part of a joint effort in Meteor observation by the Swiss "Fachgruppe Meteorastronomie" (`http://www.meteorastronomie.ch/`), which runs a network of meteor observing stations in Switzerland and is active in promoting different aspect of meteor astronomy (path determination, fireball reporting, visual, photographic, video and radio observation). Numerous discussions within this group helped in refining this project.

Note added in proof

A spectrum calibration method similar to (Ceplecha, 1961) can be found in (Zender et al., 2014) which includes distortion caused by an image intensifier.

References

Calabretta M. R. and Greisen E. W. (2002). "Representations of celestial coordinates in FITS". *Astronomy and Astrophysics*, **395:3**, 1077–1122.

Ceplecha Z. (1961). "Determination of wave-lengths in meteor spectra by using a diffraction grating". *Bulletin of the Astronomical Institute of Czechoslovakia*, **12:6**, 246–250.

Kwon M.-K., Colas F., Vaubaillon J., Birlan M., Zanda B., Marmo C., Bouley S., Audureau Y., Vernazza P., and Gattacceca J. (2014). "Astrometry with fish eye lens and orbit determination". In *Proceedings of the International Meteor Conference, Giron, France, 18-21 September 2014*. pages 42–43.

Rendtel J. (2002). *Handbook of photographic meteor observation*. IMO.

Rowland H. A. (1893). "Gratings in theory and practice". *Astronomy and astro-physics / Goodsell Observatory*, **12**, 129–149.

Schroeder D. J. (1970). "Design considerations for astronomical echelle spectrograph". *Publications of the Astronomical Society of the Pacific*, **82:490**, 1253–1275.

Zender J., Koschny D., and Ravensberg K. (2014). "Calibration of spectral video observations in the visual: theoretical overview of the ViDAS calibration pipeline". In *Proceedings of the International Meteor Conference, Poznan, Poland, 22-25 August 2013*. pages 126–129.

Handling Editor: Javor Kac

Meteor spectroscopy during the 2015 Quadrantids

Bill Ward[1]

Spectroscopic video observations during the Quadrantid meteor shower 2015 were made with Watec low light level video cameras fitted with 12 mm $f/0.8$ lenses carrying 50 mm square diffraction gratings. Four spectra with adequate signal to noise ratios were captured and the results analysed and discussed.

Received 2015 April 30

1 Introduction

The Quadrantid meteor shower takes place between January 1 to 5 (Rendtel & Arlt, 2014) with a sharp maximum around January 3/4. Due to frequently poor winter weather in the northern hemisphere the observing conditions for this shower are usually not good. Combined with a very sharp maximum it is often missed.

In 2015 the conditions at the observing location in Kilwinning, North Ayrshire were good. There were clear skies during most of the night on January 3/4. However there was some interruption by cloud between $01^{h}30^{m}$ and $03^{h}30^{m}$ UT. The near full moon significantly hampered visual observing but had little effect on the video cameras. A total of 58 meteors were captured by the wide field video system, 44 being Quadrantids and 14 others. 14 Spectra were captured by the spectroscopic video cameras. Of these, four were bright enough to extract useful spectrum graphs from. Those four spectra are the subject of this paper.

2 Equipment and Methods

A battery of four Watec video cameras was deployed. Three were 902H2 Ultimate cameras carrying 12 mm $f/0.8$ lenses with 50 mm square diffraction gratings attached (2×600 groove/mm and 1×300 groove/mm). A fourth camera, a Watec 910 HX/RC was used with a 3.5–8 mm $f/1$ zoom lens. This was set to approximately 7 mm focal length and was used to monitor the meteor shower in general.

The three spectroscopic cameras were mounted on a single tripod and positioned to cover a region approximately 20–30 degrees from the radiant. The cameras were arranged such that the gratings were oriented with the axis of diffraction perpendicular to the anticipated meteor paths. However as the radiant moves with time, some of the meteors improve their dispersion aspect whilst others degrade. This is a problem of all fixed video meteor observing systems. The fields of view also had some overlap. This proved fortunate as some captures were caught on both 600 groove/mm and 300 groove/mm systems. This allowed the best dispersion aspect or most complete spectrum to be selected.

The camera video outputs were taken to PC's fitted with on-board video capture cards, 8 bit PAL, 720×568 pixel frame. The video feed was run through the motion detection software UFOCapture (SonotaCo, 2013).

[1]Email: William.Ward@glasgow.ac.uk

IMO bibcode WGN-434-ward-quadrantids
NASA-ADS bibcode 2015JIMO...43..102W

3 The Spectra

Of the fourteen meteor spectra captured four produced images bright enough to generate spectra with a reasonable signal to noise ratio. Several meteors were captured of one by one or more video camera. The videos with the best spectrum characteristics were chosen. Thus the results here are for two spectra captured with a camera carrying a 600 l/mm grating (Q1 and Q3) and two captured with a 300 l/mm grating system (Q2 and Q4).

Each spectrum is produced in a multi-step process. Firstly the composite video frame is geometrically rotated and de-slanted by the astronomical image processing package, Iris (Buil, 2014). Once in a suitable format it is imported to the spectrum processing software Visual Spec (Desnoux, 2015). The spectrum is orientated thus; the dispersion axis is realigned horizontally with the spectrum lines positioned vertically and running blue to red from left to right along the x-axis. Visual Spec bins the spectral lines to maximise the signal to noise ratio. After calibration the output graph is generated. Calibration is done using the zero order image, where available, and prominent known atmospheric lines such as the Oxygen line at 777.4 nm. This gives a measure of wavelength dispersion per pixel. Once this dispersion factor is determined, it can be used to identify lines by measuring from known lines.

The dispersion for the 300 groove/mm grating on a 12 mm $f/0.8$ lens was measured at 2.28 nm/pixel and for the 600 groove/mm gratings on a similar 12 mm $f/0.8$ lens was measured at 1.13 nm/pixel. The actual spectrum resolution achieved is heavily influenced by the native dispersion aspect and the subsequent geometric manipulation required to re-format the image for spectrum processing. The resolution was determined to be of the order of 3 nm at best by measuring the Full Width Half Maximum (FWHM) of the distinct lines in the blue part of the spectrum in Q1. Q2–Q4 were all of lower resolution. The FWHM of the magnesium line in Q2–Q3 varied between 8 nm and 11 nm. It should also be noted that the Q3 spectrum is very "noisy" due to interline readout noise from the video sensor during the re-orientation process.

However, despite these limitations, the spectroscopic analysis still gives sufficient line information for a relative comparison of the spectra to be made. The video composite frames and resulting spectrum plots of the four meteors are shown in Figures 1 to 8. Several lines of note have been identified and indicated on the spectrum plots.

Figure 1 – Q1 Video composite spectrum image.

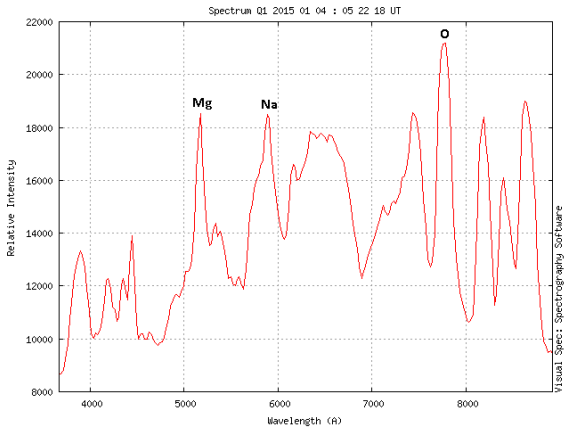

Figure 2 – Q1 meteor spectrum plot.

Figure 3 – Q2 Video composite spectrum image.

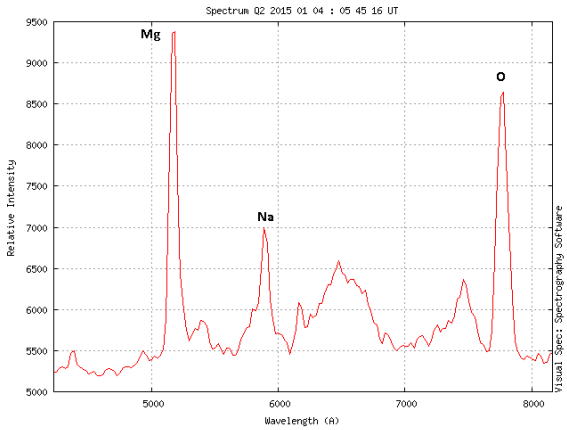

Figure 4 – Q2 meteor spectrum plot.

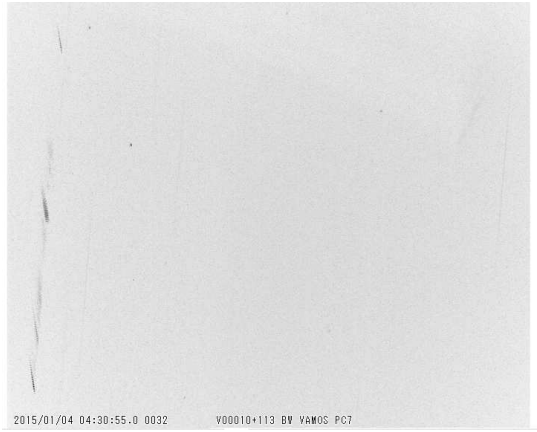

Figure 5 – Q3 Video composite spectrum image.

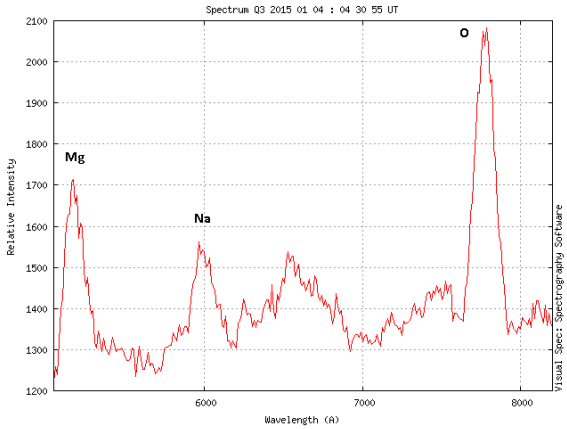

Figure 6 – Q3 meteor spectrum plot.

Figure 7 – Q4 Video composite spectrum image.

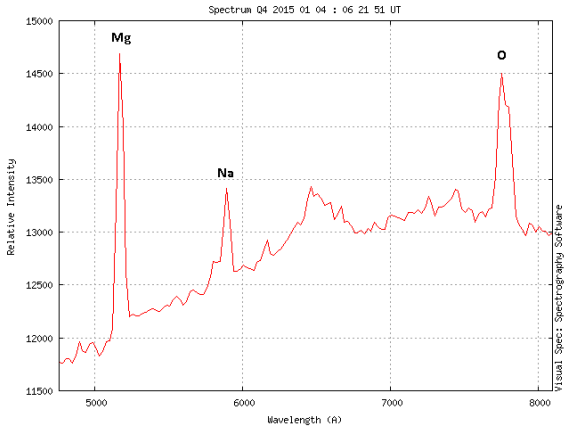

Figure 8 – Q4 meteor spectrum plot.

NOTE: The graphs are plotted without instrument correction. Fundamentally dividing all the graphs by the same flux corrected source would not materially change the result so was felt an unnecessary step in this case.
Initially Q1 stood out as an exceptionally bright capture and was processed first. The others are not in time order due to the way the various frames were selected and processed from each PC.

4 Discussion

Searching the literature revealed only one reference specific to Quadrantid meteor spectroscopy, a 2005 paper by Abe et al. One of the images from that paper is shown in Figure 9.

There was remarkable similarity in appearance of this meteor spectrum image to the negative image of Q1 as shown in Figure 10.

Initially this was taken as confirmation that Q1 was indeed a Quadrantid. However as Q2, Q3 and Q4 were reduced and the final spectra produced, it became apparent that Q1 had a significantly different appearance. In particular, the relative size of the magnesium and sodium lines showed large differences.

Comparing the spectrum plots it can be seen in Q2, Q3 and Q4 that the magnesium lines at $\sim$ 518 nm (5180Å) are significantly stronger (in relative units) than the sodium lines at $\sim$ 589 nm (5890Å). Both the magnesium triplet and sodium doublet are blended together and unresolved at this resolution. By contrast, Q1 has a much more complex spectrum with the magnesium and sodium lines being of similar strength.

The meteor trails were then examined using the UFOAnalyser software (SonotaCo, 2015). UFOAnalyser uses the positional data from the captured video to determine an angular velocity which is then used to calculate a geocentric velocity. It then matches this to the contained database to assign a possible shower membership. Whilst multi-station observations are needed to confirm shower membership without ambiguity it is nevertheless a useful guide when only single station observations are available, as in this case.

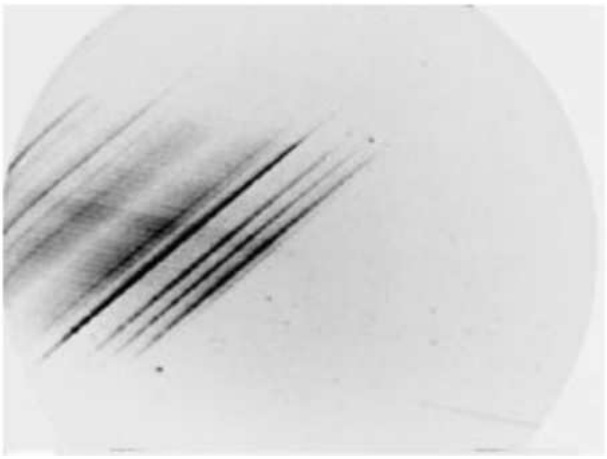

Figure 9 – Quadrantid. Figure 1 from Abe et al. (2005).

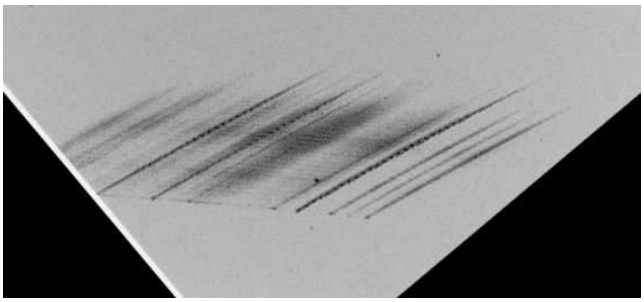

Figure 10 – Negative Quadrantid 2015 image, Bill Ward, Kilwinning, UK.

UFOAnalyser suggested that Q1 was a magnitude −6 sporadic with a velocity much higher than a typical Quadrantid, being approximately 65 km/s as compared to 41 km/s for typical Quadrantids (Rendtel & Arlt, 2014). This is subject to errors in position caused by image aberrations and limited reference stars for the software to conduct the astrometry from. While the result is indicative of Q1 not being a Quadrantid it is impossible to say so without ambiguity.

In ideal circumstances it would be preferable to have multi station observations to determine velocities better and an orbit for each of the captured meteors. However since this was not possible it was taken that alignment with the Quadrantid radiant combined with the velocity assignment generated by UFOAnalyser was sufficient for the other three meteors. Although the spectra of the other three were weaker than Q1 they were significantly different with respect to the magnesium and sodium lines.

If Q1 was not a Quadrantid, do the other spectra indicate that members of the Quadrantid meteor shower show a distinct and unique composition? If Q1 was a Quadrantid being significantly brighter and presumably a larger particle, is this is indicating some change in ablation characteristics with size? This in turn might suggest that there is some threshold at which the spectral signatures change from Q2, Q3 and Q4 to the type displayed by Q1. Borovicka (2005), discusses the distinction between "small" and "large" meteoroid ablation characteristics. His size distinction of around 1 cm is probably too great for direct comparison with the results presented here but does suggest that there may indeed be ablation effects that depend on the size of the meteoroid particle.

During a further online search, a posting on the SonotaCo meteor forum (Maeda, 2015) was noted. This was of an observation of a Quadrantid meteor and its spectrum from Japan by Koji Maeda on 2015 January 4. This is shown in Figure 11.

By processing the spectrum image in the same manner as the others it is clear that it shows very similar magnesium and sodium characteristics as Q2–Q4. It also shows prominent iron emissions in the blue. The spectrum plot is shown in Figure 12.
(It should be noted that Koji Maeda was one of the co-authors of (Buil, 2014).)

5 Conclusions

Four spectra secured during the peak of the 2015 Quadrantid meteor shower have been presented. One of the spectra, Q1, was initially assumed to be a Quadrantid. However, subsequent analysis suggests it may not be due to differences revealed by its computed geocentric velocity, this being 65 km/s, as compared to the typical Quadrantid velocity of 41 km/s (Rendtel & Arlt, 2014). Also, comparing its spectrum to the other three possible Quadrantids, Q2–Q4, showed a significant difference in the relative strengths of the magnesium and sodium

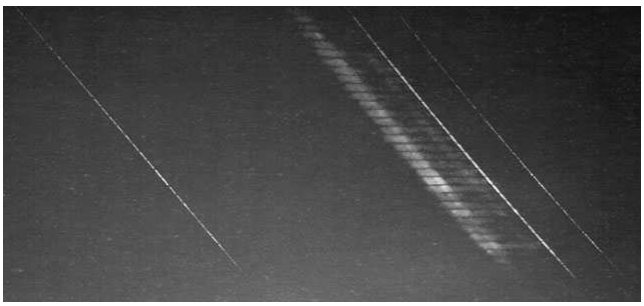

Figure 11 – Quadrantid meteor by Koji Maeda.

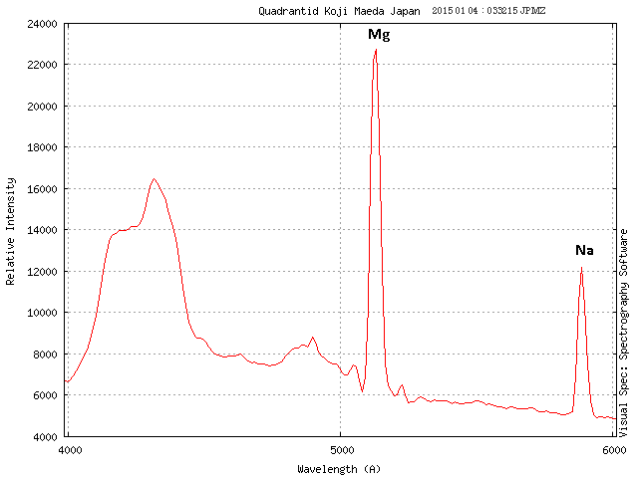

Figure 12 – Meteor spectrum by Koji Maeda.

lines. The spectra of the other three meteors (Q2–Q4) revealed that they appear to have a similar and distinct composition.

An observation of another 2015 Quadrantid from Japan also clearly indicated a stronger magnesium emission similar to that observed in the meteors Q2–Q4.

The observations also illustrate the need for multi station observations to fully remove ambiguity from observations that otherwise may result in possibly erroneous stream assignment/identification.

6 Further Work

Further observations of the Quadrantid shower will be necessary to reveal whether the spectra described here are general to the Quadrantids or perhaps represent a particular sub group of meteoroid particles within the Quadrantid stream.

In order to determine stream membership conclusively multi-station observations are needed. Much spectroscopic work has concentrated on specific campaigns observing showers such the Leonids, Geminids and Perseids. "Lesser" showers have had very little attention until recently and regular long term meteor spectroscopic surveys such as the one now run by the author seem to be much rarer than the usual meteor/fireball networks. For full characterisation combined orbital and spectrum observations are needed.

There is much to explore in meteor spectroscopy which until now has been much neglected due to instrument and technical difficulties. However these difficulties have been overcome to such a degree that regular video meteor spectroscopy is now a viable observational pursuit.
(Since this paper was submitted for review the first successful spectro-orbital observations from the UK have been made by the author and Dr David Anderson. See (Ward, 2015) for details.)

Suggested further reading:
For a detailed examination of Quadrantid orbital and parent body information see (Jenniskens, 2006).

References

Abe S., Borovicka J., Maeda K., Ebizuka N., and Watanabe J. I. (2005). "First results of Quadrantid meteor spectrum". In *Conference proceedings 36th Annual Lunar and Planetary Science Conference, March 14-18, 2005. League City, Texas.* Abstract 1536.

Borovicka J. (2006). "Physical and chemical properties of meteoroids as deduced from observations". In Daniela L., Sylvio Ferraz M., and Angel F. J., editors, *Asteroids, Comets, Meteors, Proceedings of the 229th Symposium of the International Astronomical Union held in Búzios, Rio de Janeiro, Brasil August 7-12, 2005*, volume 229. pages 249–271.

Buil C. (2014). "IRIS Astronomical image processing software". `http://www.astrosurf.com/buil/us/iris/iris.htm` .

Desnoux V. (2015). "Visual Spec spectroscopy processing software". `http://www.astrosurf.com/vdesnoux/howto.html` .

Jenniskens P. (2006). *Meteor Showers and their Parent Comets.* CUP, 357-376 pages.

Maeda K. (2015). "Qua". `http://sonotaco.jp/forum/viewtopic.php?p=37887#37887` . SonotaCo Network Japan Forum.

Rendtel J. and Arlt R., editors (2014). *Handbook For Meteor Observers.* International Meteor Organization.

SonotaCo (2013). "UFOCapture". `http://sonotaco.com/soft/e_index.html#ufocv2` .

SonotaCo (2015). "UFOAnalyser". `http://sonotaco.com/soft/e_index.html#ufoa` .

Ward B. (2015). "Spectro-orbital observation of a sporadic meteor". *WGN, Journal of the IMO*, **43:4**, 106–108.

Handling Editor: Javor Kac

Spectro-orbital observation of a sporadic meteor

Bill Ward[1]

Working in conjunction with members of the Network for Meteor Triangulation and Orbit Determination (Nemetode) arrangements were made to overlap camera fields of view. This was in an attempt to secure spectroscopic observations combined with multi station observations to determine orbits. This has resulted in the first such combined observations to be made from the UK.

Received 2015 May 1

1 Introduction

With the arrival of inexpensive low light level video cameras, numerous meteor observing networks have developed over the last several years and much reported in *WGN*.

Combined with sophisticated software, it is now possible to determine orbits of meteors captured by two or more cameras on a routine basis.

To achieve a fuller understanding of the Earth's meteoroid environment information about the physical composition of the meteors is useful. This can be arrived at by using spectroscopic techniques which allow the elements present in the meteoroid to be determined as it ablates in the atmosphere.

2 Video Meteor Spectroscopy

Video meteor spectroscopy is an extension of normal video meteor observing by the simple inclusion of a diffractive element in front of the main lens. Normally this is a diffraction grating mounted in a holder that is attached to the lens using a threaded filter holder (Figure 1). The gratings usually have between 300 and 1200 lines per millimetre and are available from any good optical supply company.

Due to the emission nature of the meteor, it effectively behaves as its own slit. That is, it forms a narrow column of light. This is then diffracted by the grating producing a spectrum, should the meteor be bright enough.

For full information on diffraction through a grating, consult (Hecht, 2002).

Whilst simple in principle, sporadic meteors are essentially random events on the sky. If they fall in the field of view, their orientation with respect to the dispersion axis of the grating is also random. (For shower meteors this can be mitigated by pre-positioning the grating dispersion axis with respect of the shower radiant). However for good dispersion a degree of luck regarding the meteor orientation is needed!

The "shallower" the spectrum with respect to the dispersion axis, the broader the lines appear. At the relatively low resolutions available, difficulties in identifying lines through poor wavelength determination/ calibration can become a serious problem. The interline read out of the video device can also add artifacts that need to be carefully dealt with.

Figure 1 – General arrangement of spectroscopic video cameras.

Once the image has been secured, it is necessary to reduce it to a form that is suitable for processing. This usually involves some geometric re-orientation and then binning to produce a spectrum plot and perhaps a colourised synthetic version for presentations purposes.

3 A Mutual Event

Having both orbital and spectrum data gives a more complete insight into the history and possible source of the meteoroid. To date this has never been achieved from Scotland (UK).

The author has been conducting video meteor spectrum observations since August 2008. Although still subject to the random nature of the meteors the quality of the spectra obtainable has improved considerably with the use of good quality 12 mm $f/0.8$ lenses and 600 lines/mm fused silica gratings.

Through the Meteor Observers Forum[a] contact was established with the coordinator and members of the NEMETODE Video Meteor Observers Group[b]. A comprehensive map of NEMETODE stations is maintained on their website. Unfortunately due to buildings, security lights, and street lighting issues the area of sky accessible to the author did not overlap with existing coverage by NEMETODE stations. An approach was made to the two nearest stations about the possibility of re-positioning their cameras (David Anderson, near Girvan and Dennis Buczynski, Tabartness).

After some seven years of experimenting (Video Atmosphere and Meteor Observation System, VAMOS and the Kilwinning Spectroscopic Survey for Meteors,

[1]Email: William.Ward@glasgow.ac.uk

IMO bibcode WGN-434-ward-sporadic
NASA-ADS bibcode 2015JIMO...43..106W

[a]http://meteorobserver.proboards.com
[b]http://www.nemetode.org

Figure 2 – Meteor and spectrum captured by B. Ward, Kilwinning, Scotland. Camera: Watec 902H2 Ultimate. Lens: 12 mm $f/0.8$, grating: 600 lines/mm (fused silica substrate).

Figure 3 – Meteor image captured by David Anderson, Low Craighead near Girvan, Scotland. Camera: Watec 902H2 Ultimate. Lens: 12 mm $f/0.8$.

KiSSMe) with different cameras, lenses, gratings, computers and all manner of accessories, there was now the possibility of achieving a step forward in routine meteor observing.

Success came more quickly than anticipated! In only a month of operation a mutual event was caught on the morning of the 2015 April 10 at $00^{h}58^{m}37^{s}$ UT. (In practical terms actually a very few hours' worth of observing!) After noting the spectrum, David was emailed and he confirmed he had got it! Figures 2 and 3 show the meteor spectra. (It was found out that Dennis had not re-orientated his camera and so did not catch the event)

4 Analysis

It was unfortunate that the meteor was relatively a bit "shallow" to the dispersion axis. Comparing the spectrum to existing examples the main lines can be identified. In this case there were prominent magnesium and sodium lines. To fit the other lines, a wavelength comparison is made using the National Institute of Standards and Technology (NIST) list as a reference. Once a wavelength calibration has been determined, the spectrum can be graphed and a synthetic version generated (Figures 4 and 5). To correct for instrument response, the spectrum has been divided through by a flux corrected black body response of 4000 K. This temperature was chosen to approximate the physical temperature of the meteor.

The spectrum shows the lines of magnesium at 518 nm (green), sodium at 589 nm (yellow) and oxygen at 777 nm (near infra red but coloured deep red for illustration). There are also bands of unresolved iron lines in the blue and green part of the spectrum. The spectrum indicates a stony mineralisation with some iron content.

Using the multi-station tracks a ground track and orbit were determined by processing the information through UFOOrbit (Figures 6 and 7).

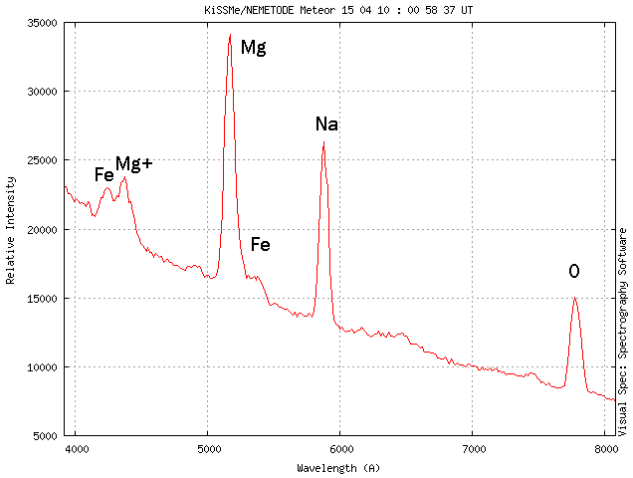

Figure 4 – Instrument response corrected spectrum graph.

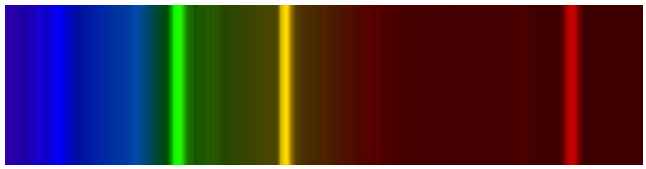

Figure 5 – Colourised synthetic spectrum.

The orbit has an inclination of approximately 10 degrees and an aphelion within the asteroid belt. This suggests the meteoroid was of asteroidal origin, perhaps a tiny fragment of a long past collision.

5 Conclusion

A mutual event has been recorded by two stations, one of which was operating a spectroscopic system. The orbit and spectrum reveal the stony (iron) composition and its source from within the asteroid belt. It is the first time that such a multi station spectro-orbital meteor observation has been conducted from Scotland (UK).

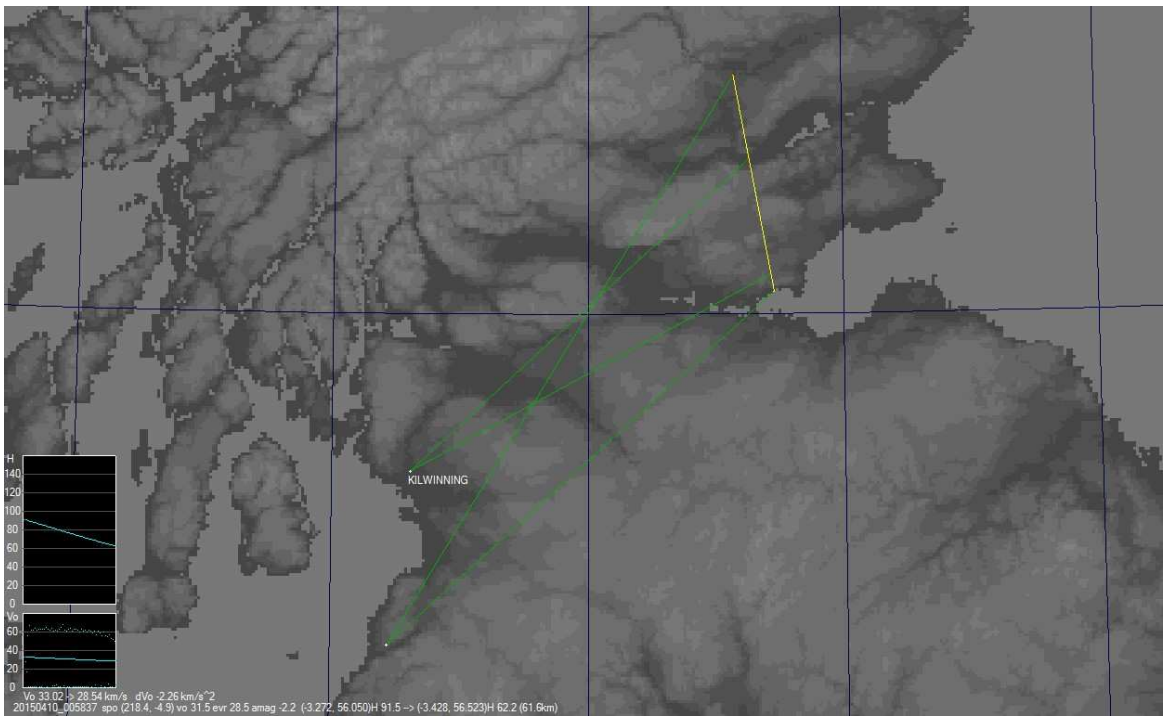

Figure 6 – Ground track of meteor as determined from the two observations.

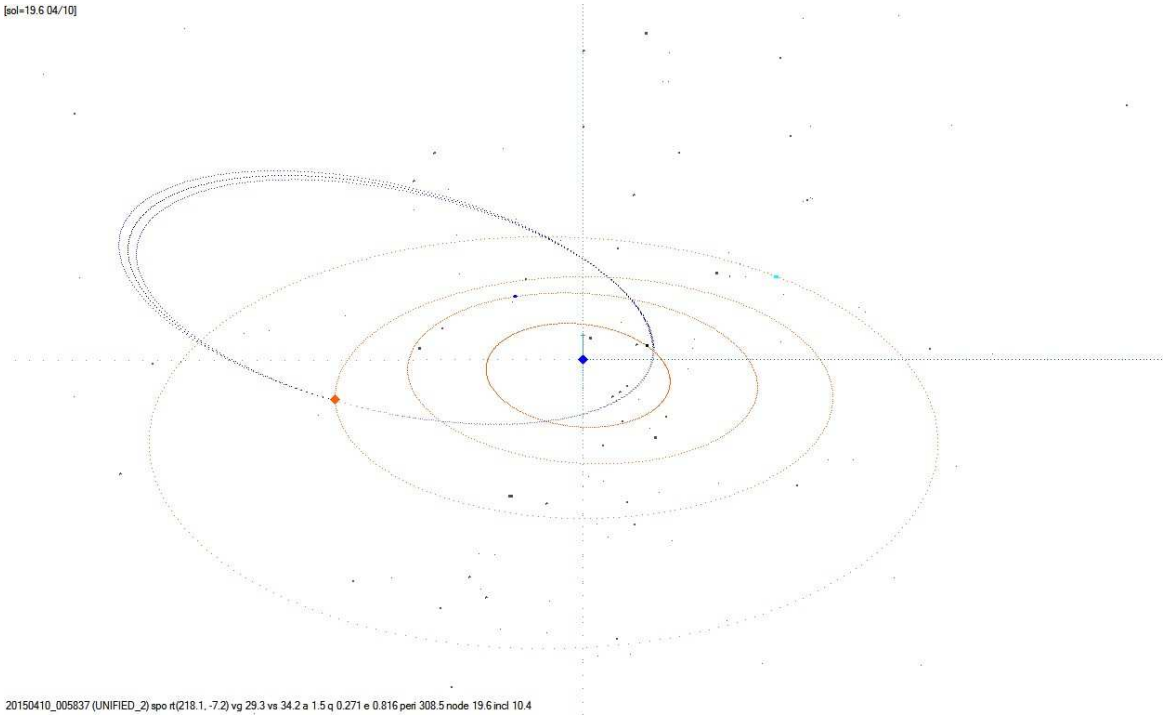

Figure 7 – 3D perspective view of the meteoroid orbit.

Acknowledgements

Observations such as this are highly collaborative ventures. Each station is individually specialised but it is only by working in tandem that these results are achievable. The author would like to express his thanks to David Anderson for his efforts and cooperation. Thanks also to Nemetode Network co-ordinator William Stewart for his support and for carrying out the orbital analysis. This work would not have been possible without the help and support of Dr Marc Sorel and Dr David Muir of the School of Engineering, University of Glasgow.

References

Hecht E. (2002). *Optics.* Addison Wesley, 476 pages.

National Institute of Standards and Technology (NIST). "Basic atomic spectroscopic data – finding list". `http://physics.nist.gov/PhysRefData/Handbook/Tables/findinglist.htm` .

Handling Editor: Javor Kac

Preliminary results

Results of the IMO Video Meteor Network — March 2015

Sirko Molau[1], *Javor Kac*[2], *Stefano Crivello*[3], *Enrico Stomeo*[4], *Geert Barentsen*[5], *Rui Goncalves*[6], *Carlos Saraiva*[7], *Maciej Maciejewski*[8], *and Mikhail Maslov*[9]

Observation statistics of the IMO Video Meteor Network for 2015 March are presented. Sporadic meteors were studied with respect to their flux density and population index profiles. Alternative methods to derive population index from video observations were explored in order to confirm or refute the outliers in the population index profile.

Received 2015 April 20

1 Introduction

Spring developed in a promising way. There were some periods where the nice weather took a time-out, but overall March was pleasant and sympathetic to the observers. Fifty out of the 84 active cameras spread over all regions managed to obtain twenty or more observing nights. Even though the total effective observing time could not quite catch up with the result of 2014, it was still the third most successful month ever with over 11 000 hours. As in previous years, the hourly average reached the annual low with just 1.7 meteors per hour, which yields a total of almost 19 000 meteors in March (Table 1 and Figure 1). Since the start of the IMO Video Meteor Network in 1999, we have recorded more than 100 000 meteors in this low-activity month, which is the best total in the first half of the year after January. All other months still have slightly less meteors.

In March, our Portuguese team added a new observer for the IMO Network. Alvaro Lopes operates a Watec 902H2 camera with 6 mm $f/0.75$ Panasonic lens in Lisbon. In Hungary another camera saw first light. Husor2 is operated by Karoly Jonas, and just like its twin camera it consists of a KTC 350BH camera with a 1/3" $f/0.95$ zoom lens from Fujinon.

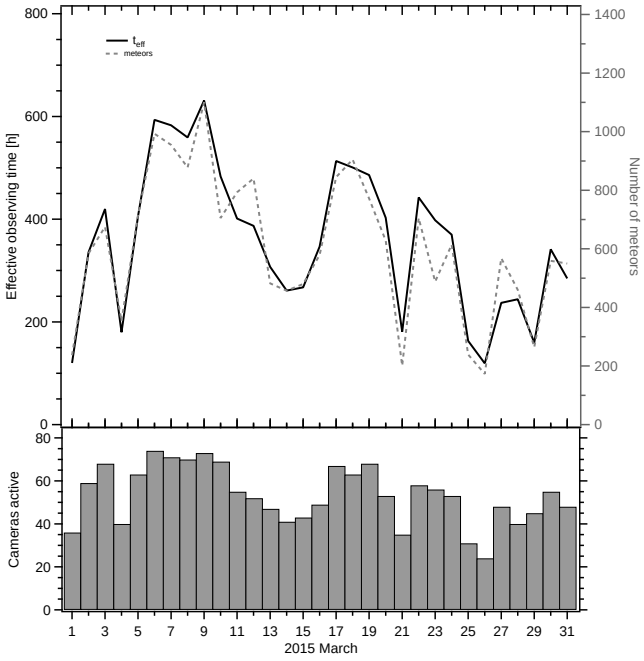

Figure 1 – Monthly summary for the effective observing time (solid black line), number of meteors (dashed gray line) and number of cameras active (bars) in 2015 March.

2 Sporadic meteors

In months without noticeable meteor activity we are clutching at straws and eventually have another look at the sporadic meteors. Due to the low activity, the data set is small, but the results cannot be affected by major showers.

The flux density profile (Figure 2) yields no surprises. The activity scatters around an average value and there are only a few outliers.

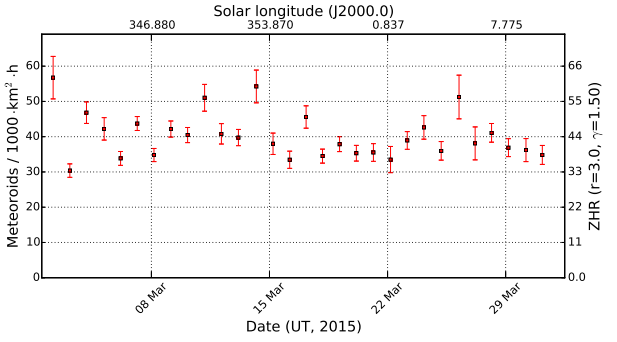

Figure 2 – Flux density profile of sporadic meteors, obtained from video observations of the IMO Network in March 2015.

[1]Abenstalstr. 13b, 84072 Seysdorf, Germany. Email: sirko@molau.de
[2]Na Ajdov hrib 24, 2310 Slovenska Bistrica, Slovenia. Email: javor.kac@orion-drustvo.si
[3]Via Bobbio 9a/18, 16137 Genova, Italy. Email: stefano.crivello@libero.it
[4]via Umbria 21/d, 30037 Scorze (VE), Italy. Email: stom@iol.it
[5]NASA Ames Research Center, M/S 244-30, Moffett Field, CA 94035, USA. Email: hello@geert.io
[6]Urbanizacao da Boavista, Lote 46, Linhaceira, 2305-114 Asseiceira, Tomar, Portugal. Email: rui.goncalves@ipt.pt
[7]Rua Aquilino Ribeiro, 23 - 1 Dto. 2790028 Carnaxide, Portugal. Email: carlos.saraiva@netcabo.pt
[8]Wolynska 24, 22-100 Chelm, Poland. Email: mazziek@gmail.com
[9]16 Bronny, 90, Novosibirsk, Russia. Email: ast3@ngs.ru

IMO bibcode WGN-434-molau-vidmar
NASA-ADS bibcode 2015JIMO...43..109M

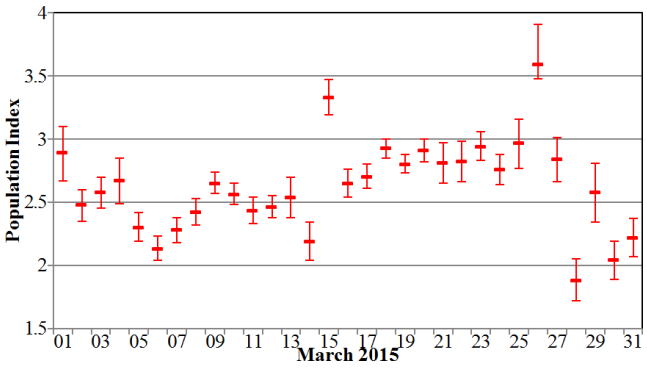

Figure 3 – Population index profile of sporadic meteors in March 2015.

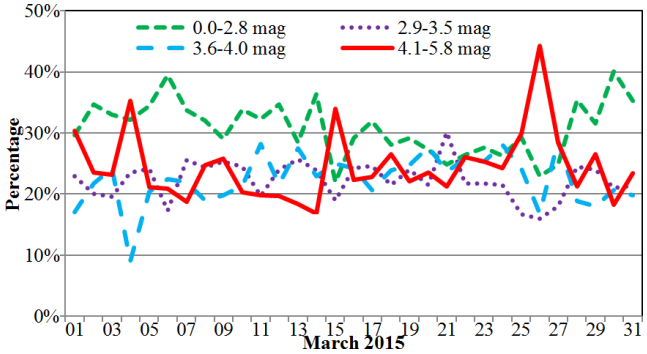

Figure 4 – Percentage of sporadic meteors in different limiting magnitude classes, each of which contains about a quarter of the effective collection areas.

More exciting is a look at the population index profile (Figure 3), and here we are again: The r-value is relatively stable over a longer period of time or shows a continuous behavior, and there are also sudden outliers. We see a flat profile between March 9 and 26, but also a downward outlier on March 14 followed by two upward outliers on March 15 and 26.

As always, the raw data are checked first: Are there any special features at these times? Is the data set particularly big or small? Are there specific cameras, which are (not) in operation in these nights?

No, the raw data show no peculiarities. If, for example, each camera in turn is taken out of the March 15 data set and the population index is recalculated without this camera, there are only minor deviations in the population index. In this particular case, taking three sensitive cameras out lowered the r-value the most, but even when all three cameras were removed at the same time, the population index was still above 3.0.

If the interim results of the population index calculation are checked it becomes clear that the most powerful cameras recorded fewer meteors on March 14, but more on March 15 and 26 than in the nights before and after. This is depicted in Figure 4. Here the observing intervals are split into four brightness classes depending on the limiting magnitude such that each class contains about a quarter of the effective collection area. Then it was checked how many meteors were recorded in each class. In most nights, the intervals with lowest limiting magnitude have the biggest share of meteors, but on March 15 and 26 suddenly the more sensitive cameras

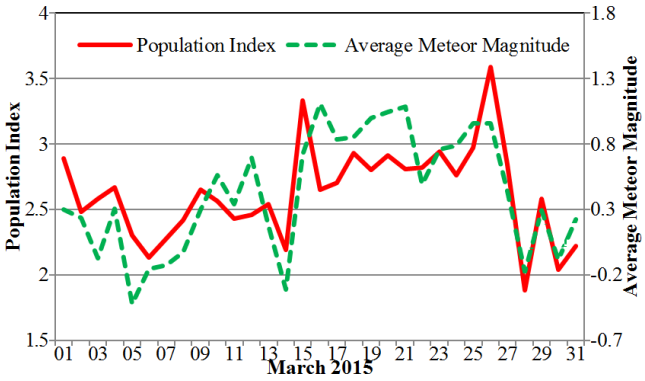

Figure 5 – Comparison of the average meteor brightness per night with the population index of sporadic meteors in March 2015.

are most successful. A large percentage of meteors from highly sensitive cameras results obviously in a larger population index, but it still does not explain why the cameras were so successful in these nights.

Since we still do not know if the outliers in the r-profile are real or just artifacts from specific boundary conditions, we looked for an independent confirmation. One option is to calculate the population index in the traditional way based on meteor magnitudes. Unfortunately we know that the accuracy of our video data is not very good in this respect, since the brightness is calculated from pixel sums in single, noisy video frames. Bright stars near the meteor trail or a bright image border may distort the result significantly. But that is not all yet – there is also a systematic error in brightness calculations. If skies are pristine, a faint meteor will yield a small pixel sum. If it is misty or cloudy such that only the brightest stars are visible, a very bright meteor that just makes it through the mist yields the same small pixel sum and brightness. The true meteor brightness is underestimated by several magnitudes. To avoid this error, all brightness measures would need to be systematically corrected by the difference between the current stellar limiting magnitude and the one when the reference image was taken. In practice that correction was neither implemented nor tested.

Still there is hope: If all meteor brightnesses are reduced to a single average value per night, the errors should mostly cancel each other out with a few hundred sporadic meteors. In addition, the number of meteors is significantly decreasing when the limiting magnitude is getting worse. If there is a loss of two magnitudes, only about ten percent of sporadic meteors are visible, such that only one out of ten meteors shows a systematic deviation of two magnitudes. So the traditional meteor brightness-based approach may at least give a hint, if the procedure that uses meteor counts of different cameras has some basic problem.

Figure 5 compares the average brightness of sporadic meteors with the population index of the same night. The average meteor magnitude was plotted against the y-axis on the right side, which is scaled such that both curves fit best. Indeed, the essential structures of the profile are all found here – the low value at the start of month, the minimum at March 14, larger values there-

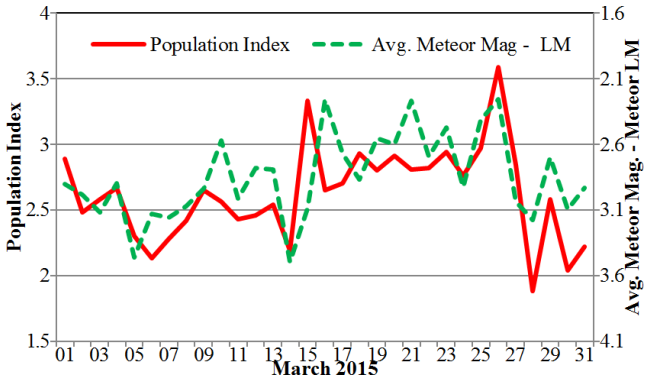

Figure 6 – Comparison of the average difference between the meteor brightness and the limiting magnitude of the camera with the population index of sporadic meteors in March 2015.

after and the breakdown towards the end of the month. That is also reflected by the relatively large Pearson's correlation coefficient of 0.74 between the two curves. The two outliers on March 15 and 26 are hardly visible, though.

Now this presentation has some flaws because it lumps cameras with different limiting magnitudes together. If a particularly sensitive camera has to pause because of clouds, the average meteor magnitude lowers automatically. That effect is intensified by the fact that sensitive cameras record more meteors. For this reason we alternatively plotted the average difference between the meteor brightness and the limiting magnitude just as done in visual observations. Note that the values of the y-axis at the right side are now in reverse order. Indeed, the profiles fit here as well and even the outliers seem to be present, but the peak on March 15 has a certain flaw: The shift by one day seems to be negligible, but it is not. The data sets from March 15 and 16 are completely independent from each other. One method yields an outlier on March 15, the other method one day later. That is not a good agreement. This may also explain why the absolute value of the correlation coefficient of -0.60 is a bit smaller (the negative sign reflects the inverse correlation).

Now how do we obtain real population indices from average meteor brightness values or differences between meteor brightness and limiting magnitude? In case of visual observations, a transformation is applied that was derived 25 years ago by Ralf Koschak and Jürgen Rendtel (1990) based on "double count" observations. With these observations it was analysed, if in case one observer spots a meteor, the other would see it as well. The result was converted into a probability to spot a meteor. In visual observation there are two important factors – the difference between the meteor brightness and the limiting magnitude (the fainter a meteor, the lower the chance to see it), and the distance from the center of the field of view (the farther away a meteor, the lower the chance to see it).

For video observations, the second factor is irrelevant, because the detection probability is the same in the full field of view. So it comes as no surprise that the visual transformation function yields no sensible result when applied directly to video data. What remains is the dependency from the difference between meteor and limiting magnitude. In our video flux density calculation, a simple step function is assumed: Up to the limiting magnitude, all meteors are detected, beyond that none. This step function still does not provide a sensible result when applied to the calculation of the population index.

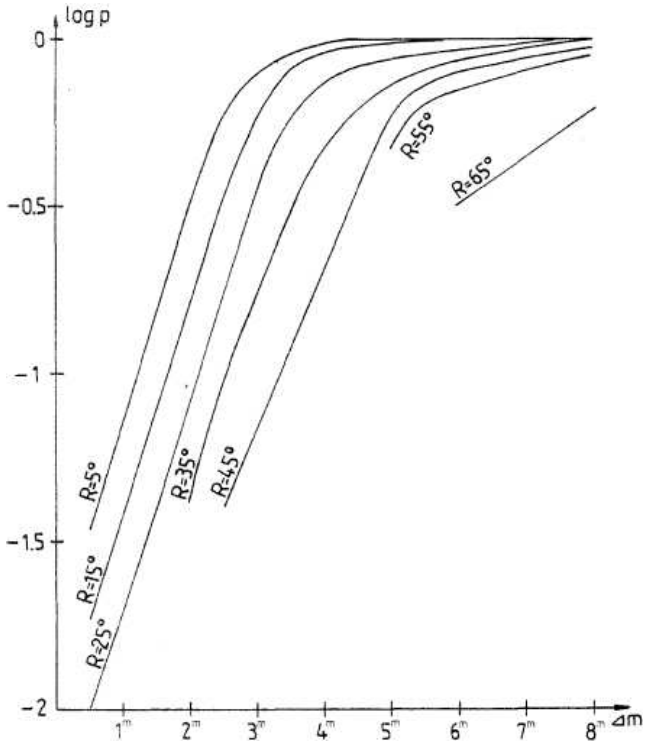

Figure 7 – Log detection probabilities for meteors depending on the difference between the meteor brightness and visual limiting magnitude (Δm) as well as the distance from the center of field of view (R). The illustration was taken from Koschak and Rendtel (1990).

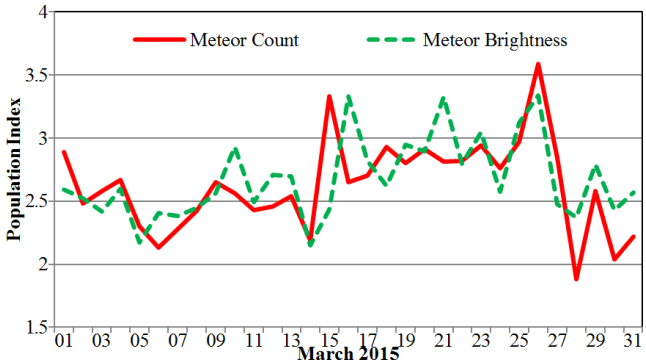

Figure 8 – Comparison of population indices of sporadic meteors in March 2015, obtained from the meteor count at different limiting magnitudes, and the meteor brightness values.

A better approach is to model the detection probability with the same type of function as in visual observation. The result of the "double count" observation was, that the log detection probability $\log P$ is growing linearly with the difference between meteor magnitude and limiting magnitude Δm (Figure 7). At the upper end the linear function is snapping off, but that is simply ignored here.

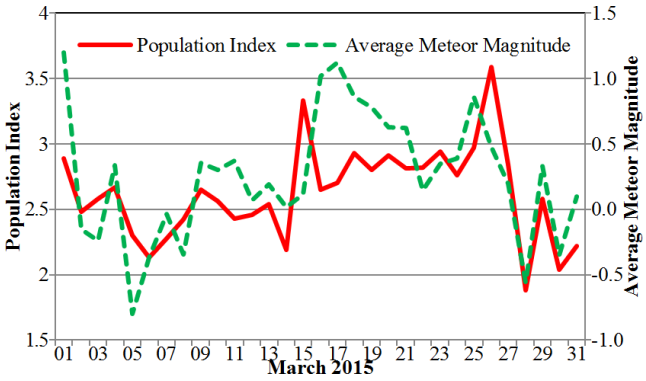

Figure 9 – Comparison of the average meteor brightness of the three strongest sporadic radiants per night with the population index of sporadic meteors in March 2015.

The dependency can alternatively be described by an exponential function of type $P = c_1 \times \Delta m^{c_2}$, where c_1 and c_2 are constants. Unfortunately Koschak and Rendtel (1990) give no formula but only a table with the raw values. These values were copied into an Excel file and an exponential respectively linear functions were fitted. As can be seen in Figure 7, all linear functions have about the same slope of 0.6. It means that the increase in detection probability with increasing brightness differences is in principle the same – the functions only deviate in the value at which the detection probability is 100%. Or to say it with other words: The bigger the distance from the center of field of view, the brighter must be a meteor to be safely detected.

Using the probability function above and with the help of a little program by Rainer Arlt it was now possible to calculate the population index from the average difference between meteor brightness and video limiting magnitude. Also at this step we obtain only a long list of values that are imported to Excel and approximated by an exponential function of type $r = c_3 \times \Delta m^{c_4}$, where c_3 and c_4 are also constants. The exponent c_4 was in many cases almost exactly -1.0. That it, r and Δm are inversely proportional and the formulae can be further simplified to $r = c_3/\Delta m$.

That is the theory for visual observations. If we take a similar transformation function $r = c_3 \times \Delta m^{c_4}$ for video observations and adjust the parameters until the population index profile fits best to the target function, we find values of $c_4 = -1$ and $c_3 = 7.5$. Hence, also video observations can apply the simplified transformation function $r = c_3/\Delta m$.

Figure 8 presents a comparison of both population index profiles. The new graph looks very similar to the one presented in Figure 6. With 0.59, also the correlation index is almost identical in both cases. That is probably because the population index and the difference between meteor brightness and limiting magnitude are inversely proportional. We may conclude that the detection probability of meteors depending on brightness difference from the limiting magnitude is comparable to visual observers at constant distance from the center of field of view. Looking at the log probabilities, we also find a linear function with a slope of roughly 0.6.

Now it only remains to be understood why in case of video observations the 100% detection probability is obtained at a larger difference between meteor and limiting magnitude than at the center of field of view of visual observers. There is also a nice explanation for this offset. The determination of the limiting magnitude in MetRec works as follows: A number of video frames are stacked, all point-like objects above the noise level are extracted, the stars are identified, and their number is transformed into a limiting magnitude by the star field counting method. To detect a meteor, on the other hand, it must be above the detection threshold in at least three consecutive video frames. The meteor brightness is then calculated from the pixel sum in individual video frames. Both algorithms are not directly comparable to each other and will yield a constant offset. In stacked video frames, fainter stars become visible and will be identified, which will systematically increase the determined limiting magnitude and thereby also increase the difference between the meteor brightness and the limiting magnitude.

To summarize: There is good reason to assume that video cameras and visual observers have the same type of dependency for the detection probability of meteors, which is inversely proportional to the difference between meteor brightness and limiting magnitude. If the average meteor brightness is compared with the population index profile, the outliers mostly disappear. However, if the limiting magnitude is considered as well, they partly show up again. That gives a hint to search for the root cause not in the algorithm used to calculate population indices, but rather in the limiting magnitude calculation of sensitive cameras.

Finally there was a last attempt to explain the outliers from data. One possible interpretation may be that in these nights a small, unknown meteor shower with large population index was active, that shifted the whole brightness distribution. To verify this hypothesis, the program RadFind was adjusted such that is calculates the mean meteor brightness for each detected radiant. Then the active radiants including their average meteor brightness were calculated for each day of March. The values from the three most active radiants (without the Antihelion source) per night were averaged and plotted in Figure 9.

The results of this type of analysis shows no peculiarities in the nights in question. So we have some new ideas but still no satisfying explanation for the outliers in the population index profile.

References

Koschack R. and Rendtel J. (1990). "Determination of spatial number density and mass index from visual meteor observations (I).". *WGN, Journal of the IMO*, **18:2**, 44–58.

Handling Editor: Javor Kac

Code	Name	Location	Camera	FOV [°²]	Stellar LM [mag]	Eff.CA [km²]	Nights	Time [h]	Meteors
ARLRA	Arlt	Ludwigsfelde/DE	Ludwig2 (0.8/8)	1475	6.2	3779	24	127.2	385
BANPE	Bánfalvi	Zalaegerszeg/HU	Huvcse01 (0.95/5)	2423	3.4	361	11	20.4	71
BERER	Berkó	Ludányhalászi/HU	Hulud1 (0.8/3.8)	5542	4.8	3847	12	106.4	293
			Hulud3 (0.95/4)	4357	3.8	876	11	76.6	69
BOMMA	Bombardini	Faenza/IT	Mario (1.2/4.0)	5794	3.3	739	21	147.7	293
BREMA	Breukers	Hengelo/NL	Mbb3 (0.75/6)	2399	4.2	699	17	127.4	119
BRIBE	Klemt	Herne/DE	Hermine (0.8/6)	2374	4.2	678	21	151.6	245
		Bergisch Gladbach/DE	Klemoi (0.8/6)	2286	4.6	1080	23	145.7	227
CASFL	Castellani	Monte Baldo/IT	Bmh1 (0.8/6)	2350	5.0	1611	25	206.2	401
			Bmh2 (1.5/4.5)*	4243	3.0	371	23	188.0	264
CRIST	Crivello	Valbrevenna/IT	Bilbo (0.8/3.8)	5458	4.2	1772	25	169.7	311
			C3P8 (0.8/3.8)	5455	4.2	1586	22	160.6	189
			Stg38 (0.8/3.8)	5614	4.4	2007	26	191.8	614
DONJE	Donani	Faenza/IT	Jenni (1.2/4)	5886	3.9	1222	18	116.1	250
ELTMA	Eltri	Venezia/IT	Met38 (0.8/3.8)	5631	4.3	2151	19	131.7	165
FORKE	Förster	Carlsfeld/DE	Akm3 (0.75/6)	2375	5.1	2154	15	105.8	221
GONRU	Goncalves	Tomar/PT	Templar1 (0.8/6)	2179	5.3	1842	27	207.2	427
			Templar2 (0.8/6)	2080	5.0	1508	27	209.9	365
			Templar3 (0.8/8)	1438	4.3	571	23	175.2	144
			Templar4 (0.8/3.8)	4475	3.0	442	25	189.0	302
			Templar5 (0.75/6)	2312	5.0	2259	26	182.4	281
GOVMI	Govedič	Središče ob Dravi/SI	Orion2 (0.8/8)	1447	5.5	1841	24	162.0	239
			Orion3 (0.95/5)	2665	4.9	2069	15	109.1	100
			Orion4 (0.95/5)	2662	4.3	1043	14	106.6	95
HERCA	Hergenrother	Tucson/US	Salsa3 (0.8/3.8)	2336	4.1	544	29	234.7	392
HINWO	Hinz	Schwarzenberg/DE	Hinwo1 (0.75/6)	2291	5.1	1819	13	102.6	249
IGAAN	Igaz	Debrecen/HU	Hudeb (0.8/3.8)	5522	3.2	620	23	173.4	146
		Hódmezővásárhely/HU	Huhod (0.8/3.8)	5502	3.4	764	22	131.1	113
		Budapest/HU	Hupol (1.2/4)	3790	3.3	475	16	135.2	37
JONKA	Jonas	Budapest/HU	Husor (0.95/4)	2286	3.9	445	23	182.2	146
			Husor2 (0.95/3.5)	2465	3.9	715	19	131.9	97
KACJA	Kac	Ljubljana/SI	Orion1 (0.8/8)	1402	3.8	331	24	155.9	101
		Kamnik/SI	Cvetka (0.8/3.8)*	4914	4.3	1842	16	112.6	256
			Rezika (0.8/6)	2270	4.4	840	19	126.8	424
			Stefka (0.8/3.8)	5471	2.8	379	18	120.2	232
		Kostanjevec/SI	Metka (0.8/12)*	715	6.4	640	1	7.8	7
KISSZ	Kiss	Sülysáp/HU	Husul (0.95/5)*	4295	3.0	355	16	95.3	40
KOSDE	Koschny	Izana Obs./ES	Icc7 (0.85/25)*	714	5.9	1464	12	61.9	339
		La Palma/ES	Icc9 (0.85/25)*	683	6.7	2951	24	151.9	792
		Noordwijkerhout/NL	Lic4 (1.4/50)*	2027	6.0	4509	21	130.5	179
LOJTO	Łojek	Grabniak/PL	Pav57 (1.0/5)	1631	3.5	269	11	73.3	50
LOPAL	Lopes	Lisboa/PT	Naso1 (0.75/6)	2377	3.8	506	10	29.1	56

Table 1 – Observers contributing to 2015 March data of the IMO Video Meteor Network. Eff.CA designates the effective collection area; the overall number of nights is the number of nights with at least one camera operating, the overall observing time and number of meteors are sums over all cameras.

Table 1 – Observers contributing to 2015 March data of the IMO Video Meteor Network – continued from previous page.

Code	Name	Location	Camera	FOV [°²]	Stellar LM [mag]	Eff.CA [km²]	Nights	Time [h]	Meteors
MACMA	Maciejewski	Chełm/PL	Pav35 (0.8/3.8)	5495	4.0	1584	22	149.3	177
			Pav36 (0.8/3.8)*	5668	4.0	1573	24	157.9	280
			Pav43 (0.75/4.5)*	3132	3.1	319	21	158.4	185
			Pav60 (0.75/4.5)	2250	3.1	281	25	153.9	358
MARGR	Maravelias	Lofoupoli-Crete/GR	Loomecon (0.8/12)	738	6.3	2698	13	78.5	60
MARRU	Marques	Lisbon/PT	Cab1 (0.8/3.8)	5291	3.1	467	20	169.6	248
			Ran1 (1.4/4.5)	4405	4.0	1241	24	143.7	242
MASMI	Maslov	Novosibirsk/RU	Nowatec (0.8/3.8)	5574	3.6	773	11	60.5	129
MOLSI	Molau	Seysdorf/DE	Avis2 (1.4/50)*	1230	6.9	6152	22	139.9	686
			Mincam1 (0.8/8)	1477	4.9	1084	22	133.2	315
		Ketzür/DE	Remo1 (0.8/8)	1467	6.5	5491	2	11.6	15
			Remo2 (0.8/8)	1478	6.4	4778	25	139.5	387
			Remo3 (0.8/8)	1420	5.6	1967	18	70.8	158
			Remo4 (0.8/8)	1478	6.5	5358	26	145.2	452
MORJO	Morvai	Fülöpszállás/HU	Huful (1.4/5)	2522	3.5	532	25	180.8	143
MOSFA	Moschner	Rovereto/IT	Rover (1.4/4.5)	3896	4.2	1292	23	34.3	138
OCHPA	Ochner	Albiano/IT	Albiano (1.2/4.5)	2944	3.5	358	13	77.0	99
OTTMI	Otte	Pearl City/US	Orie1 (1.4/5.7)	3837	3.8	460	18	121.1	133
PERZS	Perkó	Becsehely/HU	Hubec (0.8/3.8)*	5498	2.9	460	25	195.2	339
PUCRC	Pucer	Nova vas nad Dragonjo/SI	Mobcam1 (0.75/6)	2398	5.3	2976	18	139.7	139
ROTEC	Rothenberg	Berlin/DE	Armefa (0.8/6)	2366	4.5	911	8	56.0	50
SARAN	Saraiva	Carnaxide/PT	Ro1 (0.75/6)	2362	3.7	381	24	175.0	214
			Ro2 (0.75/6)	2381	3.8	459	26	216.0	302
			Ro3 (0.8/12)	710	5.2	619	28	223.1	425
			Sofia (0.8/12)	738	5.3	907	26	189.9	203
SCHHA	Schremmer	Niederkrüchten/DE	Doraemon (0.8/3.8)	4900	3.0	409	21	128.5	235
SLAST	Slavec	Ljubljana/SI	Kayak1 (1.8/28)	563	6.2	1294	24	165.2	142
			Kayak2 (0.8/12)	741	5.5	920	22	175.2	88
STOEN	Stomeo	Scorze/IT	Min38 (0.8/3.8)	5566	4.8	3270	23	149.4	355
			Noa38 (0.8/3.8)	5609	4.2	1911	24	166.3	366
			Sco38 (0.8/3.8)	5598	4.8	3306	24	170.7	420
STRJO	Strunk	Herford/DE	Mincam2 (0.8/6)	2354	5.4	2751	21	124.7	184
			Mincam3 (0.8/6)	2338	5.5	3590	19	122.8	171
			Mincam4 (1.0/2.6)	9791	2.7	552	22	115.5	108
			Mincam5 (0.8/6)	2349	5.0	1896	19	120.6	158
			Mincam6 (0.8/6)	2395	5.1	2178	22	128.6	138
TEPIS	Tepliczky	Agostyán/HU	Huago (0.75/4.5)	2427	4.4	1036	25	196.9	191
			Humob (0.8/6)	2388	4.8	1607	24	169.9	329
TRIMI	Triglav	Velenje/SI	Sraka (0.8/6)*	2222	4.0	546	21	54.0	131
YRJIL	Yrjölä	Kuusankoski/FI	Finexcam (0.8/6)	2337	5.5	3574	10	73.9	110
ZELZO	Zelko	Budapest/HU	Huvcse03 (1.0/4.5)	2224	4.4	933	12	63.5	65
			Huvcse04 (1.0/4.5)	1484	4.4	573	1	7.6	4
* active field of view smaller than video frame						Overall	31	11 124.1	18 798

Results of the IMO Video Meteor Network — April 2015

Sirko Molau[1], *Javor Kac*[2], *Stefano Crivello*[3], *Enrico Stomeo*[4], *Geert Barentsen*[5], *Rui Goncalves*[6], *Carlos Saraiva*[7], *Maciej Maciejewski*[8], *and Mikhail Maslov*[9]

In 2015 April, 86 cameras of the IMO Video Meteor Network recorded over 25 000 meteors in more than 10 000 hours of observing time. Flux density profiles of the Lyrids are presented, covering the years 2012–2015. The peak rate is reached at $\lambda_\odot = 32°$. Population index profile is presented for the Lyrids, with values fluctuating between $r = 2.0$ and 2.5 in the nights around the peak rate.

Received 2015 July 11

1 Introduction

The first few months of 2015 had already been promising, but the observing conditions improved further in April. With 86 cameras active overall we are slowly approaching one hundred video systems. Two thirds of these cameras managed to collect data on twenty or more nights, and no region was particularly advantaged or disadvantaged. On several nights there were more than 75 active cameras, and the all-time high was reached on April 10 with 79 video cameras.

For the third time already in 2015 we were able to accumulate more than 10 000 hours of effective observing time in one month, which is 40% more than in the best April so far. With over 25 000 meteors, the output of the IMO Video Meteor Network even grew by more than half compared to last April (Table 1 and Figure 1).

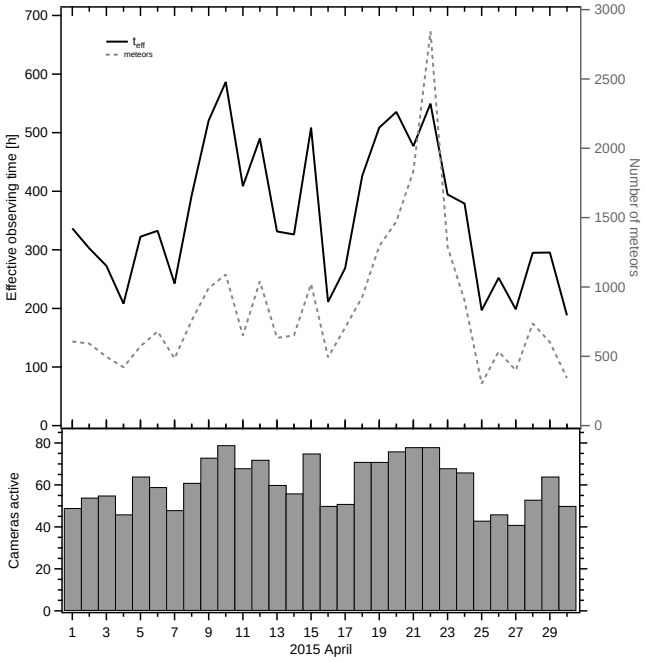

Figure 1 – Monthly summary for the effective observing time (solid black line), number of meteors (dashed gray line) and number of cameras active (bars) in 2015 April.

2 Lyrids

After a break of over three months, there was finally a meteor shower with significant activity again. The 2015 flux density profile of the Lyrids fits well to the data of the previous three years (Figure 2). The ascent starts at about 30° solar longitude. The peak is reached slightly after $\lambda_\odot = 32°$ (in the evening hours UT of 2015 April 22), and at 34° solar longitude the activity has ceased. The descending activity branch is slightly shallower than the ascending branch. The flux density peaks almost constantly at 4 meteoroids per 1 000 km^2 per hour.

Next we analysed the brightness distribution of the Lyrids. Figure 3 shows the population index profile of the sporadic meteors and Lyrids. The profile for the sporadic meteors is similar to that for March – the r-value fluctuates between 2.5 and 3.0 with a few outliers. The population index of the Lyrids is smaller by 0.5 to 0.6 throughout, i.e. there is a larger fraction of bright meteors. However the population index is still higher than in the previous year when we found values below 2.0 in the nights preceding and following the peak night (Molau et al., 2014).

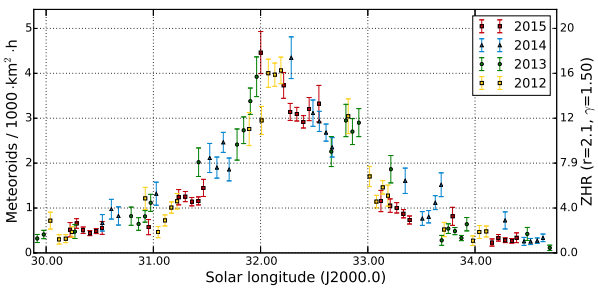

Figure 2 – Flux density profile of the Lyrids, obtained from video observations of the IMO Network in April 2012–2015.

[1]Abenstalstr. 13b, 84072 Seysdorf, Germany. Email: sirko@molau.de
[2]Na Ajdov hrib 24, 2310 Slovenska Bistrica, Slovenia. Email: javor.kac@orion-drustvo.si
[3]Via Bobbio 9a/18, 16137 Genova, Italy. Email: stefano.crivello@libero.it
[4]via Umbria 21/d, 30037 Scorze (VE), Italy. Email: stom@iol.it
[5]NASA Ames Research Center, M/S 244-30, Moffett Field, CA 94035, USA. Email: hello@geert.io
[6]Urbanizacao da Boavista, Lote 46, Linhaceira, 2305-114 Asseiceira, Tomar, Portugal. Email: rui.goncalves@ipt.pt
[7]Rua Aquilino Ribeiro, 23 - 1 Dto. 2790028 Carnaxide, Portugal. Email: carlos.saraiva@netcabo.pt
[8]Wolynska 24, 22-100 Chelm, Poland. Email: mazziek@gmail.com
[9]16 Bronny, 90, Novosibirsk, Russia. Email: ast3@ngs.ru

IMO bibcode WGN-434-molau-vidapr
NASA-ADS bibcode 2015JIMO...43..115M

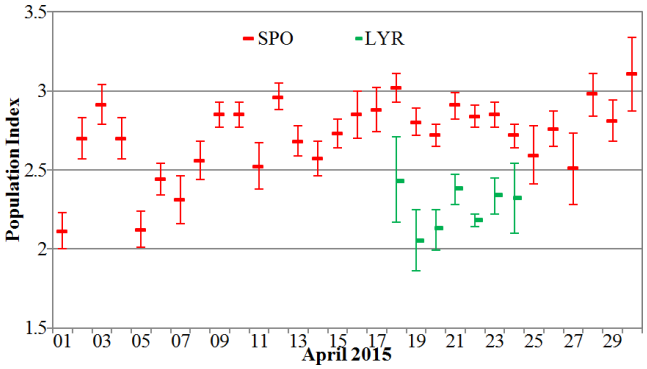

Figure 3 – Population index profile of the Lyrids and sporadic meteors in April 2015.

Near the turn of the year 2014/2015 we had analysed whether the population index calculation can be improved by using extremely sensitive meteor cameras and thereby extending the limiting magnitude range. The result was that the benefit of these cameras is limited by their low yield on meteors. Nevertheless Sirko Molau's camera Escimo2 started regular observation in April with a 25 mm $f/0.85$ Fujinon lens (field of view $14° \times 11°$, limiting magnitude $> +8$ mag). The aim was not to throw the data into the big pool collected in the IMO Network, but to use them primarily for the population index calculation.

The main idea was as follows: The effective collection area, i.e. how many square kilometers of the atmosphere at what limiting magnitude a video camera is monitoring, is a prime ingredient in the calculation of flux densities and population indices. Among others, the effective collection area is calculated from the limiting magnitude of the camera, the altitude of the field of view, and the angular velocity of meteors. If there are systematic errors (e.g. due to not properly accounting for the extinction near the horizon or due to determining an average limiting magnitude over the full field of view), individual cameras may distort the overall result and cause scatter of the r-value. To minimize the impact of these systematic errors, Escimo2 was mounted exactly in parallel to Mincam1 (field of view $43° \times 32°$, limiting magnitude +6 mag). Hence, both cameras have the same center of field of view, the same distance from the radiant resp. the same meteor angular velocity, the same boundary conditions regarding lunar distance, cloudiness, and more. Only the size of the field of view and the limiting magnitude differ, and therefore the difference in limiting magnitude should be constant thanks to the identical observing direction. For this reason, an alternative method to calculate the population index can be applied, as was presented at IMC 2014 (Molau, 2014) to explain the principle of the population index calculation: The r-value can be derived directly from the meteor count ratio of both cameras!

The new camera Escimo2 was installed just in time for the Lyrid maximum, and the night sky was almost completely clear between April 18/19 and 24/25. As an example, Figure 4 shows a Lyrid that was recorded by both cameras on April 24. The image was inverted for better contrast.

When configuring the new camera the first problem emerged: The initial value of the "NoiseLevel" parameter has a significant impact on the limiting magnitude that is calculated for the camera.

What does that mean? To determine the limiting magnitude, an averaged background image is compared against a threshold: Pixels that are by the amount "NoiseLevel" brighter than their surroundings are segmented as stars and identified by the software. That threshold has to be adjusted dynamically to take into account the camera and observing conditions: The noisier the video image, the larger must be the threshold. If it is set to the right value, the majority of segmented objects can be identified and only a small remaining number are particularly noisy pixels. If the threshold is reduced, the number of identified stars slowly increases, since even fainter stars are recognized. At the same time, the number of unidentified "stars" (i.e. noisy pixels) grows over-proportionally. If the threshold is increased, on the other hand, the number of identified stars will slowly reduce, but the number of noisy pixels will reduce more quickly. The automated adjustment of the threshold is programmed such that a certain ratio between identified stars and noisy pixels is reached. Furthermore this ratio is dependent on the star count. If only few stars are identified, a large fraction of noisy pixels is allowed. If there are hundreds of identified stars, the percentage of noisy pixels must become smaller.

It turned out that over a certain range of thresholds the ratio of identified stars and noisy pixels remains approximately constant, i.e. that both the number of identified stars and noisy pixels increases or decreases by about the same amount when the threshold is adapted. Changing the start value of the threshold will lead to the algorithm converging on a different number of stars and hence to report a different limiting magnitude. In the actual case, the difference was about half a magnitude, which has a significant impact on the calculated flux density and population index. We have to think again how the algorithm can be improved. Maybe it should not target for a certain ratio but rather for an absolute number of noisy pixels.

Further testing was carried out with both cameras using the same start value for "NoiseLevel", and the results showed that the profiles of both cameras were similar. Figure 5 shows the development of the limiting magnitude on April 22/23 and 24/25. There were short breaks due to cloud on both nights, and we saw two interesting effects: On the one hand, the drop in limiting magnitude lasts a little longer for Mincam1 compared to Escimo2. That is understandable given the larger field of view where clouds enter earlier and remain longer. Even more interesting is the behavior of Escimo2 at dawn – under clear skies the limiting magnitude is reported to be increasing instead of decreasing. That must be caused by the electronics of the camera. It is a simple fact that more stars are identified for Escimo2 in morning twilight than under dark skies. It is also a fact that Escimo2 is on average 2.3 mags more sensitive than Mincam1.

We next investigated how the effective collection area of the cameras (and hence the number of expected Lyrids n_{Lyr}) depends on the population index r_{Lyr}. This dependency was calculated for different nights and we can see that the relationship is indeed almost identical in all nights. Hence the assumption is correct, that from the population index alone we can derive the expected ratio of meteors for both cameras (Figure 6 left). Now the function only needed to be inverted, and there you go: From the observed ratio of recorded meteors you can calculate the population index (Figure 6 right). Of course that is not magic, because the population index is by definition the ratio of cumulative meteor counts under different meteor limiting magnitudes. Anyhow, an exponential function was fitted to the profile, and for this particular pair of cameras we obtained the following formula: $r_{\mathrm{Lyr}} = 7.6664 \times (\frac{n_{\mathrm{Lyr,Mincam1}}}{n_{\mathrm{Lyr,Escimo2}}}) - 0.841$.

Now only the number of meteors that both cameras had recorded per night needed to be plugged into the formula ... and then, disaster!

We obtained totally unbelievable r-values, which could be easily reconstructed: Figure 7 (left) shows the raw number of Lyrids recorded by Mincam1 and Escimo2 per night. The graph of Mincam1 shows the expected increase to up to 25 Lyrids in the peak night, followed by a decrease. Escimo2, on the other hand, recorded constantly between 0 and 2 Lyrids on every night. There is no sign whatsoever of the Lyrid peak!

And it got even worse: Figure 7 (right) shows the number of sporadic meteors on the same nights. Here the values of Mincam1 is scattering as expected around a constant value, whereas Escimo2 shows an increase by almost a factor of two towards April 21/22, and a declining meteor count thereafter.

Most people would assume that there must be a problem with the meteor shower assignment procedure of Escimo2, but that is not the case: The meteor plot of the peak night (Figure 8) shows that all but two backward prolongations of meteors recorded by Escimo2 clearly miss the Lyrid radiant.

We had expected a result of lower accuracy due to the low meteor count of Escimo2, since the accuracy is governed by the effective collection area of the camera. However, that the Lyrid peak cannot be seen at all in the meteor counts of Escimo2 was a big surprise.

There are two possible ways forward: On the one hand we can wait for a more active shower like the Perseids, when Escimo2 will hopefully record a sufficient number of meteors. On the other hand, error sources can further be eliminated by giving Escimo2 a lens with the same focal length and a slower f-stop than Mincam1, in place of the lens that had the same f-stop and longer focal length. Then the fields of view would be fully identical and there would be no need to calculate an effective collection area at all. The population index could instead be calculated directly from the difference in limiting magnitude lm and the ratio of meteor counts:

$$r_{\mathrm{Lyr}} = \left(\frac{n_{\mathrm{Lyr,Mincam1}}}{n_{\mathrm{Lyr,Escimo2}}} \right)^{\frac{1}{(lm_{\mathrm{Escimo2}} - lm_{\mathrm{Mincam1}})}}$$

Hence there is further room for experiments and improvements.

References

Molau S. (2014). "Meteor showers identified from one million video meteors". In Gyssens M., Roggemans P., and Zoladek P., editors, *Proceedings of the International Meteor Conference, Poznan, Poland, 22-25 August 2013*. pages 26–38.

Molau S., Kac J., Crivello S., Stomeo E., Barentsen G., Goncalves R., and Igaz A. (2014). "Results of the IMO Video Meteor Network – April 2014". *WGN, Journal of the IMO*, **42:4**, 145–149.

Handling Editor: Javor Kac

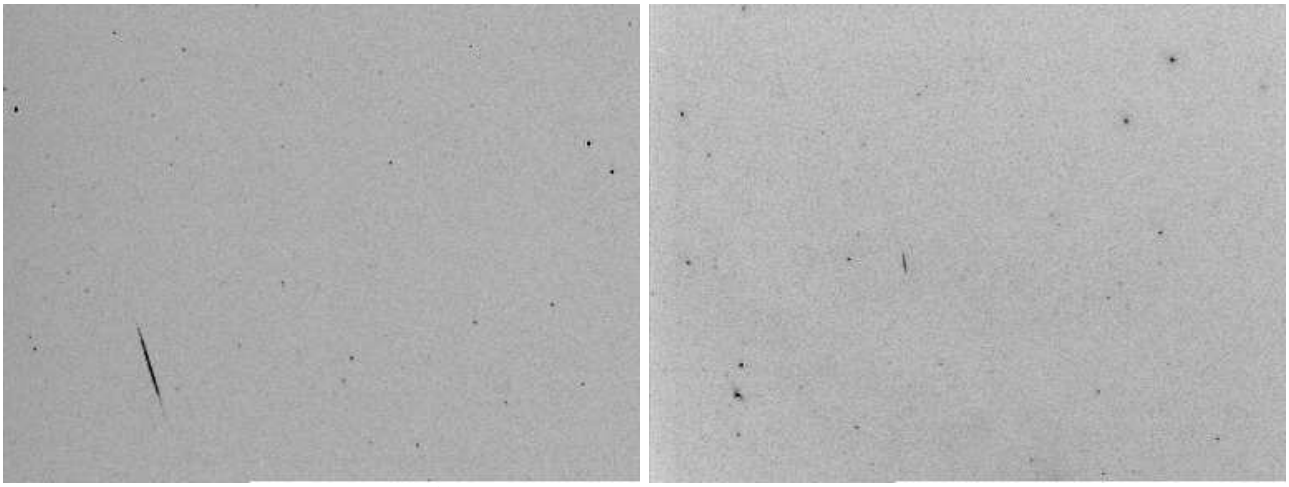

Figure 4 – Lyrid on 2015 April 24 at $01^{\mathrm{h}}21^{\mathrm{m}}$ UT, recorded by the cameras Escimo2 (left) and Mincam1 (right) which are mounted in parallel.

Code	Name	Location	Camera	FOV [°²]	Stellar LM [mag]	Eff.CA [km²]	Nights	Time [h]	Meteors
ARLRA	Arlt	Ludwigsfelde/DE	Ludwig2 (0.8/8)	1475	6.2	3779	28	151.1	645
BANPE	Bánfalvi	Zalaegerszeg/HU	Huvcse01 (0.95/5)	2423	3.4	361	16	12.4	76
BERER	Berkó	Ludányhalászi/HU	Hulud1 (0.8/3.8)	5542	4.8	3847	15	105.2	405
			Hulud3 (0.95/4)	4357	3.8	876	13	99.1	98
BOMMA	Bombardini	Faenza/IT	Mario (1.2/4.0)	5794	3.3	739	22	147.6	463
BREMA	Breukers	Hengelo/NL	Mbb3 (0.75/6)	2399	4.2	699	23	144.4	180
BRIBE	Klemt	Herne/DE	Hermine (0.8/6)	2374	4.2	678	26	170.7	288
		Bergisch Gladbach/DE	Klemoi (0.8/6)	2286	4.6	1080	26	172.4	290
CASFL	Castellani	Monte Baldo/IT	Bmh1 (0.8/6)	2350	5.0	1611	24	191.1	473
			Bmh2 (1.5/4.5)*	4243	3.0	371	23	181.2	330
CRIST	Crivello	Valbrevenna/IT	Bilbo (0.8/3.8)	5458	4.2	1772	21	164.0	346
			C3P8 (0.8/3.8)	5455	4.2	1586	20	133.7	219
			Stg38 (0.8/3.8)	5614	4.4	2007	21	174.3	691
DONJE	Donani	Faenza/IT	Jenni (1.2/4)	5886	3.9	1222	22	170.9	565
ELTMA	Eltri	Venezia/IT	Met38 (0.8/3.8)	5631	4.3	2151	22	142.7	273
FORKE	Förster	Carlsfeld/DE	Akm3 (0.75/6)	2375	5.1	2154	22	137.6	325
GONRU	Goncalves	Tomar/PT	Templar1 (0.8/6)	2179	5.3	1842	26	162.2	344
			Templar2 (0.8/6)	2080	5.0	1508	25	141.7	269
			Templar3 (0.8/8)	1438	4.3	571	22	138.1	97
			Templar4 (0.8/3.8)	4475	3.0	442	24	137.4	268
			Templar5 (0.75/6)	2312	5.0	2259	26	124.5	218
GOVMI	Govedič	Središče ob Dravi/SI	Orion2 (0.8/8)	1447	5.5	1841	24	130.0	330
			Orion3 (0.95/5)	2665	4.9	2069	12	54.2	60
			Orion4 (0.95/5)	2662	4.3	1043	17	55.8	118
HERCA	Hergenrother	Tucson/US	Salsa3 (0.8/3.8)	2336	4.1	544	28	227.4	392
HINWO	Hinz	Schwarzenberg/DE	Hinwo1 (0.75/6)	2291	5.1	1819	22	145.1	371
IGAAN	Igaz	Debrecen/HU	Hudeb (0.8/3.8)	5522	3.2	620	23	141.6	203
		Hódmezővásárhely/HU	Huhod (0.8/3.8)	5502	3.4	764	24	151.9	164
		Budapest/HU	Hupol (1.2/4)	3790	3.3	475	18	120.2	49
JONKA	Jonas	Budapest/HU	Husor (0.95/4)	2286	3.9	445	27	179.3	167
			Husor2 (0.95/3.5)	2465	3.9	715	25	157.8	141
KACJA	Kac	Ljubljana/SI	Orion1 (0.8/8)	1402	3.8	331	24	135.4	136
		Kamnik/SI	Cvetka (0.8/3.8)*	4914	4.3	1842	17	109.2	446
			Rezika (0.8/6)	2270	4.4	840	17	109.7	600
			Stefka (0.8/3.8)	5471	2.8	379	16	96.3	267
		Kostanjevec/SI	Metka (0.8/12)*	715	6.4	640	1	6.4	4
KISSZ	Kiss	Sülysáp/HU	Husul (0.95/5)*	4295	3.0	355	26	161.4	106
KOSDE	Koschny	Izana Obs./ES	Icc7 (0.85/25)*	714	5.9	1464	24	156.9	935
		La Palma/ES	Icc9 (0.85/25)*	683	6.7	2951	25	181.1	1224
		Noordwijkerhout/NL	Lic4 (1.4/50)*	2027	6.0	4509	23	130.6	219
LOJTO	Łojek	Grabniak/PL	Pav57 (1.0/5)	1631	3.5	269	13	79.2	78
LOPAL	Lopes	Lisbon/PT	Naso1 (0.75/6)	2377	3.8	506	18	15.7	90

Table 1 – Observers contributing to 2015 April data of the IMO Video Meteor Network. Eff.CA designates the effective collection area; the overall number of nights is the number of nights with at least one camera operating, the overall observing time and number of meteors are sums over all cameras.

Table 1 – Observers contributing to 2015 April data of the IMO Video Meteor Network – continued from previous page.

Code	Name	Location	Camera	FOV [°²]	Stellar LM [mag]	Eff.CA [km²]	Nights	Time [h]	Meteors
MACMA	Maciejewski	Chełm/PL	Pav35 (0.8/3.8)	5495	4.0	1584	22	88.0	322
			Pav36 (0.8/3.8)*	5668	4.0	1573	27	118.7	388
			Pav43 (0.75/4.5)*	3132	3.1	319	20	132.9	203
			Pav60 (0.75/4.5)	2250	3.1	281	24	94.2	395
MARGR	Maravelias	Lofoupoli-Crete/GR	Loomecon (0.8/12)	738	6.3	2698	17	96.8	167
MARRU	Marques	Lisbon/PT	Cab1 (0.8/3.8)	5291	3.1	467	25	149.0	197
			Ran1 (1.4/4.5)	4405	4.0	1241	17	100.6	140
MASMI	Maslov	Novosibirsk/RU	Nowatec (0.8/3.8)	5574	3.6	773	10	44.8	105
MOLSI	Molau	Seysdorf/DE	Avis2 (1.4/50)*	1230	6.9	6152	25	160.6	994
			Escimo2 (0.85/25)	155	8.1	3415	16	113.7	209
			Mincam1 (0.8/8)	1477	4.9	1084	25	151.0	548
		Ketzür/DE	Remo1 (0.8/8)	1467	6.5	5491	26	160.3	742
			Remo2 (0.8/8)	1478	6.4	4778	28	164.0	684
			Remo3 (0.8/8)	1420	5.6	1967	10	57.9	127
			Remo4 (0.8/8)	1478	6.5	5358	29	169.7	771
MORJO	Morvai	Fülöpszállás/HU	Huful (1.4/5)	2522	3.5	532	26	183.2	184
MOSFA	Moschner	Rovereto/IT	Rover (1.4/4.5)	3896	4.2	1292	21	24.9	169
OCHPA	Ochner	Albiano/IT	Albiano (1.2/4.5)	2944	3.5	358	21	160.4	196
OTTMI	Otte	Pearl City/US	Orie1 (1.4/5.7)	3837	3.8	460	24	144.4	183
PERZS	Perkó	Becsehely/HU	Hubec (0.8/3.8)*	5498	2.9	460	23	167.7	348
PUCRC	Pucer	Nova vas nad Dragonjo/SI	Mobcam1 (0.75/6)	2398	5.3	2976	15	102.7	135
ROTEC	Rothenberg	Berlin/DE	Armefa (0.8/6)	2366	4.5	911	21	104.9	231
SARAN	Saraiva	Carnaxide/PT	Ro1 (0.75/6)	2362	3.7	381	24	115.4	165
			Ro2 (0.75/6)	2381	3.8	459	21	113.0	179
			Ro3 (0.8/12)	710	5.2	619	20	121.1	247
			Sofia (0.8/12)	738	5.3	907	22	87.2	115
SCHHA	Schremmer	Niederkrüchten/DE	Doraemon (0.8/3.8)	4900	3.0	409	22	127.0	257
SLAST	Slavec	Ljubljana/SI	Kayak1 (1.8/28)	563	6.2	1294	23	106.4	281
			Kayak2 (0.8/12)	741	5.5	920	23	154.2	116
STORO	Štork	Ondřejov/CZ	Ond1 (1.4/50)*	2195	5.8	4595	23	141.8	382
STOEN	Stomeo	Scorze/IT	Min38 (0.8/3.8)	5566	4.8	3270	25	168.6	451
			Noa38 (0.8/3.8)	5609	4.2	1911	24	165.2	537
			Sco38 (0.8/3.8)	5598	4.8	3306	2	7.6	121
STRJO	Strunk	Herford/DE	Mincam2 (0.8/6)	2354	5.4	2751	24	144.2	270
			Mincam3 (0.8/6)	2338	5.5	3590	25	135.4	245
			Mincam4 (1.0/2.6)	9791	2.7	552	26	131.6	173
			Mincam5 (0.8/6)	2349	5.0	1896	26	152.5	239
			Mincam6 (0.8/6)	2395	5.1	2178	25	141.9	220
TEPIS	Tepliczky	Agostyán/HU	Huago (0.75/4.5)	2427	4.4	1036	24	181.7	202
			Humob (0.8/6)	2388	4.8	1607	28	133.7	388
TRIMI	Triglav	Velenje/SI	Sraka (0.8/6)*	2222	4.0	546	22	85.6	165
YRJIL	Yrjölä	Kuusankoski/FI	Finexcam (0.8/6)	2337	5.5	3574	17	72.8	140
ZELZO	Zelko	Budapest/HU	Huvcse03 (1.0/4.5)	2224	4.4	933	7	18.2	39
			Huvcse04 (1.0/4.5)	1484	4.4	573	9	18.2	34
						Overall	30	10 761.2	25 367

* active field of view smaller than video frame

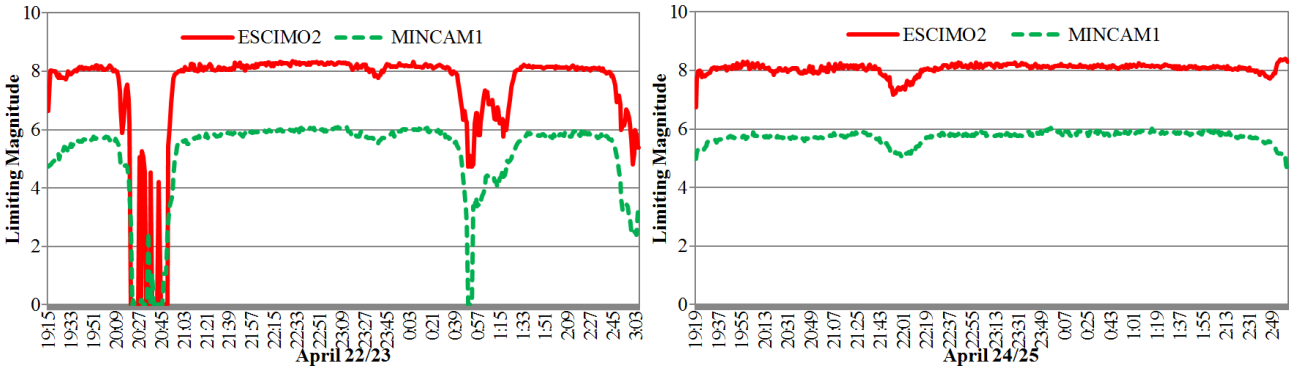

Figure 5 – Development of the limiting magnitude of Escimo2 and Mincam1 on 2015 April 22/23 and 24/25.

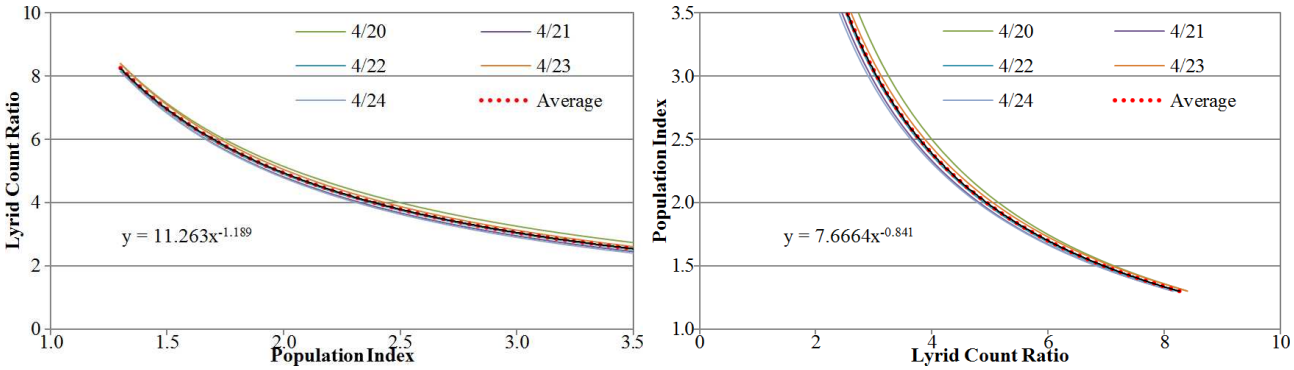

Figure 6 – Dependence of the ratio of the effective collection area (resp. the expected number of Lyrids) of Escimo2 and Mincam1 from the population index (left). On the right side, the inverse function is shown.

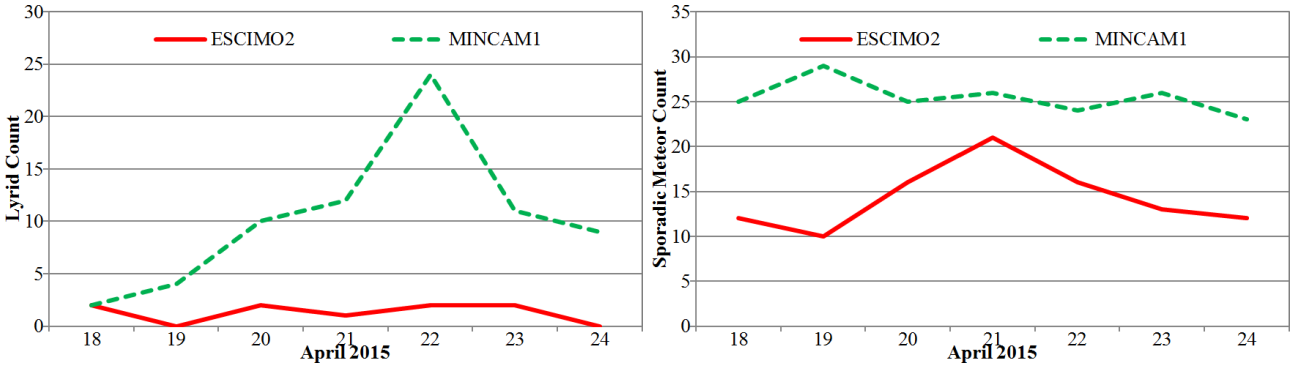

Figure 7 – Raw number of Lyrids and sporadic meteors, recorded by an Escimo2 and Mincam1 in April 2015.

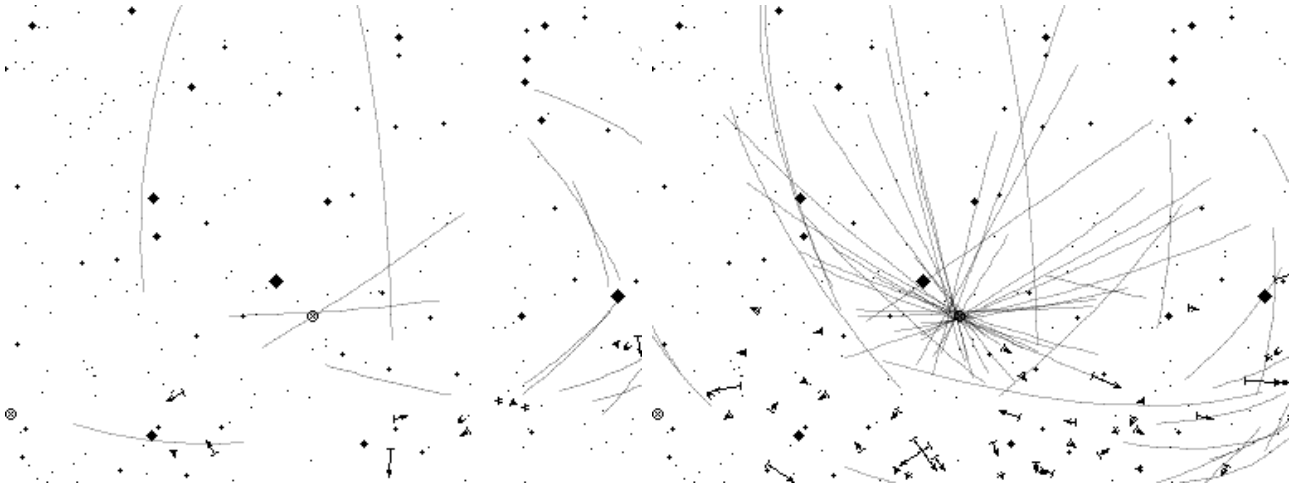

Figure 8 – Meteor backward prolongation plot of Escimo2 and Mincam1 on 2015 April 22/23.

The International Meteor Organization

web site http://www.imo.net

Council

President: Cis Verbeeck,
Bogaertsheide 5, 2560 Kessel, Belgium.
e-mail: cis.verbeeck@scarlet.be

Vice-President: Jürgen Rendtel,
Eschenweg 16, D-14476 Marquardt, Germany.
tel. +49 33208 50753
e-mail: jrendtel@aip.de

Secretary-General: Robert Lunsford,
1828 Cobblecreek Street, Chula Vista,
CA 91913-3917, USA. tel. +1 619 585 9642
e-mail: lunro.imo.usa@cox.net

Treasurer: Marc Gyssens, Heerbaan 74,
B-2530 Boechout, Belgium.
e-mail: marc.gyssens@uhasselt.be
BIC: GEBABEBB
IBAN: BE30 0014 7327 5911
Always state BIC and IBAN codes together!
Check international transfer charges with your bank; you are responsible for paying these.

Other Council members:

David Asher, Armagh Observatory, College Hill, Armagh, Northern Ireland BT61 9DG, UK.
e-mail: dja@arm.ac.uk

Geert Barentsen, NASA Ames Research Center, M/S 244-30, Moffett Field CA 94035, USA.
e-mail: hello@geert.io

Javor Kac (see details under WGN)

Detlef Koschny, Zeestraat 46,
NL-2211 XH Noordwijkerhout, Netherlands.
e-mail: detlef.koschny@esa.int

Sirko Molau, Abenstalstraße 13b, D-84072 Seysdorf, Germany. e-mail: sirko@molau.de

Jean-Louis Rault, Société Astronomique de France, 16, rue de la Vallée, 91360 Epinay sur Orge, France. e-mail: f6agr@orange.fr

Paul Roggemans (see details under IMC Liaison Officer)

Commission Directors

Visual Commission: Rainer Arlt (rarlt@aip.de)
Generic e-mail address: visual@imo.net
Electronic visual report form:
http://www.imo.net/visual/report/electronic

Video Commission: Sirko Molau (sirko@molau.de)
Generic e-mail address: video@imo.net

Photographic Commission: Bill Ward
(William.Ward@glasgow.ac.uk)
Generic e-mail address: photo@imo.net

Radio Commission: Jean-Louis Rault (f6agr@orange.fr)
Generic e-mail address: radio@imo.net

Fireballs: Online fireball reports:
http://fireballs.imo.net

IMC Liaison Officer

Paul Roggemans, Pijnboomstraat 25, 2800 Mechelen, Belgium, e-mail: paul.roggemans@gmail.com

WGN

Editor-in-chief: Javor Kac
Na Ajdov hrib 24, SI-2310 Slovenska Bistrica, Slovenia. e-mail: wgn@imo.net;
include METEOR in the e-mail subject line

Editorial board: Ž. Andreić, M. Argo, D.J. Asher, J. Correira, M. Gyssens, H.V. Hendrix, C. Hergenrother, T. Markham, J. Rendtel, J.-L. Rault, P. Roggemans, C. Verbeeck.

IMO Sales

Available from the Treasurer or the Electronic Shop on the IMO Website	€	$
IMO membership, including subscription to WGN Vol. 43 (2015)		
Surface mail	26	39
Air Mail (outside Europe only)	49	69
Electronic subscription only	21	29
Back issues of WGN on paper (price per complete volume)		
Vols. 26 (1998) – 35 (2007) except 30 (2002), 38 (2010) – 42 (2014)	15	23
Vols. 37 (2009) – 42 (2014) – electronic version only	9	13
Proceedings of the International Meteor Conference on paper		
1990, 1991, 1993, 1995, 1996, 1999, 2000, 2002, 2003, per year	9	13
2007, 2010, 2011, per year	15	23
2012, 2013, 2014 per year	25	37
Proceedings of the Meteor Orbit Determination Workshop 2006	15	23
Radio Meteor School Proceedings 2005	15	23
Handbook for Meteor Observers	15	23
Meteor Shower Workbook	12	18
Electronic media		
Meteor Beliefs Project CD-ROM	6	9
DVD: WGN Vols. 6–30 & IMC 1991, 1993–96, 2001–04	45	69

Bright fireball on 2015 July 21 over France

A very bright sporadic fireball appeared over France on 2015 July 21 at $23^{h}55^{m}28^{s}$ UT and was captured by the cameras of BOAM (Base des Observateurs Amateurs de Météores/Meteor Amateur Observers Database, `http://boam.fr`).

Christophe Demeautis, Bollwiller, Alsace, France

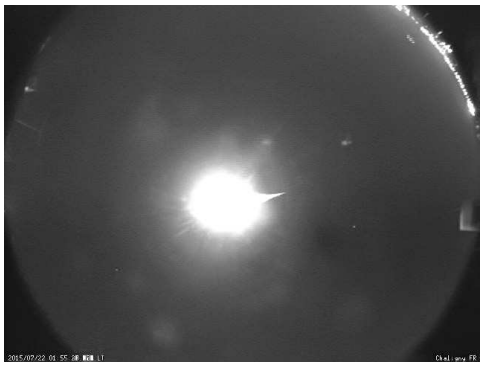

Marc Herrault, Chaligny, Lorraine, France

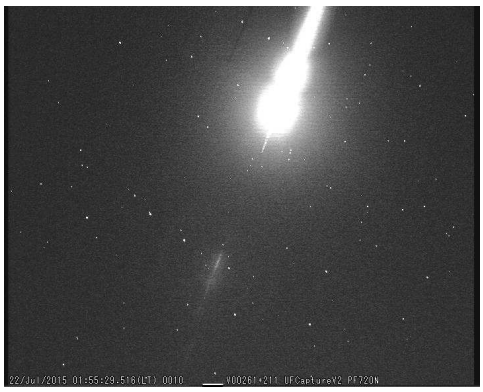

Image communicated by Karl Antier

Fireball persistent train evolution was captured from the town of Saxon-Sion, Lorraine, France using Canon EOS 650D camera set at ISO 12800 equipped with 18 mm $f/3.5$ lens, and exposures of between 19 s and 47 s. The sequence spans over 4 minutes and 15 seconds. Photos courtesy of Didier Walliang / Société Astronomique de Lorraine.